Publisher's PDF, also known as Version of record

Link to publication record in Explore Bristol Research
PDF-document

University of Bristol - Explore Bristol Research
General rights

JGR Planets

RESEARCH ARTICLE

Special Section:
InSight at Mars

Key Points:
- We infer the tectonic setting in Cerberus Fossae on Mars by seismic source inversion
- We present a robust inversion strategy for single-station moment tensor inversion
- Three Marsquakes recorded by InSight reveal a predominantly normal faulting regime

Correspondence to:
N. Brinkman,
nienke.brinkman@erdw.ethz.ch

Author Contributions:
Writing – original draft: Nienke Brinkman

First Focal Mechanisms of Marsquakes

Nienke Brinkman[1] [iD], Simon C. Stähler[1] [iD], Domenico Giardini[1] [iD], Cédric Schmelzbach[1] [iD], Amir Khan[1,2] [iD], Alice Jacob[3] [iD], Nobuaki Fuji[3] [iD], Clement Perrin[3] [iD], Philippe Lognonné[3] [iD], Eric Beucler[4] [iD], Maren Böse[1], Savas Ceylan[1] [iD], Constantinos Charalambous[5] [iD], John F. Clinton[6], Martin van Driel[1] [iD], Fabian Euchner[1] [iD], Anna Horleston[7] [iD], Taichi Kawamura[8], Brigitte Knapmeyer-Endrun[9], Guenole Mainsant[10], Mark P. Panning[11] [iD], William T. Pike[5], John-Robert Scholz[12] [iD], Johan O. A. Robertsson[1] [iD], and William B. Banerdt[11] [iD]

[1]Institute of Geophysics, ETH Zürich, Zürich, Switzerland, [2]Physik-Institut, University of Zürich, Zürich, Switzerland, [3]Institut de Physique du Globe de Paris, Université de Paris, Paris, France, [4]Laboratoire de Planétologie et Géodynamique, UMR6112, Univ. Nantes, Univ. Angers, CNRS, Nantes Cedex 3, France, [5]Department of Electrical and Electronic Engineering, Imperial College London, South Kensington Campus, London, UK, [6]Swiss Seismological Service, ETH Zürich, Zürich, Switzerland, [7]School of Earth Sciences, University of Bristol, Bristol, UK, [8]Université de Paris, Institut de Physique du Globe de Paris, CNRS, Paris, France, [9]Bensberg Observatory, University of Cologne, Bergisch Gladbach, Germany, [10]Institut Supérieur de l'Aéronautique et de l'Espace SUPAERO, Toulouse, France, [11]NASA Jet Propulsion Laboratory, California Institute of Technology, Pasadena, CA, USA, [12]Max Planck Institute for Solar System Research, Göttingen, Germany

Abstract Since February 2019, NASA's InSight lander is recording seismic signals on the planet Mars, which, for the first time, allows to observe ongoing tectonic processes with geophysical methods. A number of Marsquakes have been located in the Cerberus Fossae graben system in Elysium Planitia and further west, in the Orcus Patera depression. We present a first study of the focal mechanisms of three well-recorded events (S0173a, S0183a, S0235b) to determine the processes dominating in the source region. We infer for all three events a predominantly extensional setting. Our method is adapted to the case of a single, multicomponent receiver and based on fitting waveforms of *P* and *S* waves against synthetic seismograms computed for the initial crustal velocity model derived by the InSight team. We explore the uncertainty due to the single-station limitation and find that even data recorded by one station constrains the mechanisms (reasonably) well. For the events in the Cerberus Fossae region (S0173a, S0235b) normal faulting with a relatively steep dipping fault plane is inferred, suggesting an extensional regime mainly oriented E-W to NE-SW. The fault regime in the Orcus Patera region is not determined uniquely because only the *P* wave can be used for the source inversion. However, we find that the *P* and weak *S* waves of the S0183a event show similar polarities to the event S0173, which indicates similar fault regimes.

Plain Language Summary As time passes, the mysterious interior of Mars is slowly being unraveled due to the detection and analysis of Marsquakes recorded with a seismograph carried by the InSight lander. Close to 400 Marsquakes have so far been identified, yet only a handful of those show similarities to earthquakes. Those earth-like events are located near the Cerberus Fossae and Orcus Patera regions. We take advantage of the similarity between Marsquakes and earthquakes and apply a methodology developed for earthquake characterization before seismic recorders became abundant on Earth. We find that the Marsquakes in these source regions are dominated by extensional rather than compressing features. This is important information to further understand what causes Marsquakes.

1. Introduction

On November 26, 2018, NASA's InSight lander successfully touched down on the Martian surface in Elysium Planitia (Figure 1). The scientific goals of InSight are to determine the interior structure, composition, and thermal state of Mars, as well as to document the present-day seismicity and impact rate. To achieve these goals, InSight carried the seismometer package SEIS (Seismic Experiment for Interior Structure) to Mars including a very broadband (VBB) and short period (SP) instrument that cover the seismic bandwidth 0.01–5 Hz (Lognonné et al., 2019). These two instruments are used to locate and classify Marsquakes, to
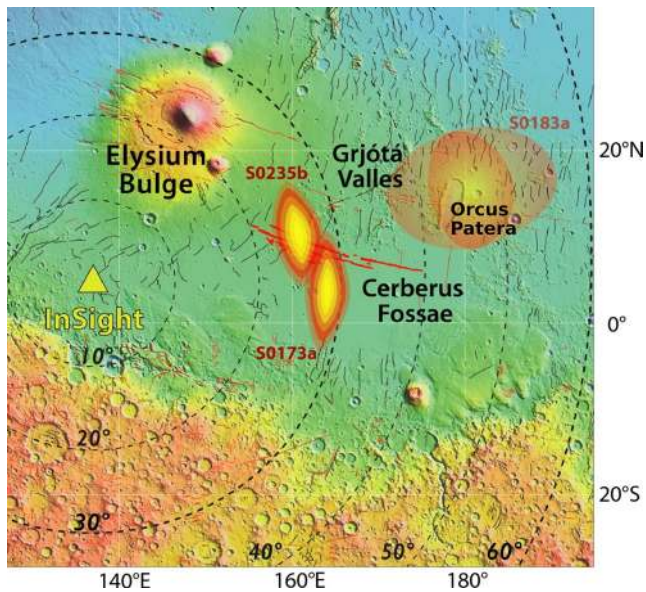
Figure 1. Mars Orbiter Laser Altimeter shaded relief of Elysium Planitia from Giardini et al. (2020). The location of the InSight lander (yellow triangle) is shown with respect to events S0235b (11°N and 161°E), S0173a (3°N and 165°E), and S0183a (23°N and 177°E) (InSight Marsquake Service, 2020). The ellipsoids indicate uncertainties in the source location. Black and red lines present reverse and normal mapped faults, respectively.

constrain the interior structure of the planet and to map its recent tectonic activity.

Up to December 31, 2019, a total of 383 seismic events have been detected by the MarsQuake Service (MQS) (Clinton et al., 2018; InSight Marsquake Service, 2020). The observed Marsquakes are assigned to four different classes ranging from A to D (Clinton et al., 2021) based on signal-to-noise ratio (SNR) and event characteristics, with class A corresponding to the highest-quality observations, clear and identifiable phases and clear polarization. Class B is similar to class A, but the signals do not show clear polarization. Signals that belong to class C are clearly visible, yet the phase picking is challenging. Class D consists of weakly observed (suspicious) signals (InSight Marsquake Service, 2020). Furthermore, the seismic events are distinguished in two categories, low-frequency (LF) events comprising recordings with energy content generally below ~1 Hz and high-frequency (HF) events corresponding to observations with dominant seismic energy above ~1 Hz (Giardini et al., 2020). So far, 40 of the 383 events are assigned to the LF category. Generally, the LF waveforms resemble recordings of terrestrial tectonic earthquakes, while most other observed events are interpreted to be very shallow regional quakes with propagation in a shallow waveguide (van Driel et al., 2020).

In this study, we are concerned with three events that occurred on sols 173, 183, and 235 (hereinafter referred to as S0173a, S0183a, and S0235b; see Table 1 for event details and Clinton et al. (2021) for details on Marsquake nomenclature and classification). These LF events belong to class A (S0173a, S0235b) and B (S0183a) in terms of SNR and are assigned magnitudes $M_w > 3$ (InSight Marsquake Service, 2020). These three Marsquakes are the only Marsquakes that have been located with sufficient confidence so far. The epicenters of these events are located in the Cerberus Fossae (S0173a and S0235b) and Orcus Patera (S0183a) regions of Elysium Planitia (Giardini et al., 2020) (see Figure 1). The Cerberus Fossae region had been considered a seismically active region on Mars prior to landing based on detailed studies of fault systems and orbital imaging of potential seismically induced rock falls (Knapmeyer et al., 2006; Roberts et al., 2012; Taylor et al., 2013). Initial analyses of the InSight seismic data confirm this expectation (Banerdt et al., 2020; Giardini et al., 2020; Lognonné et al., 2020). The tectonic regime of Cerberus Fossae is understood as an extensional graben system driven by the weight of Elysium Mons (Taylor et al., 2013). In contrast, relatively little is known about Orcus Patera, a 700 km long depression, but interpretations range from an oblique impact crater to a volcanic caldera (van der Kolk et al., 2001).

The focal mechanism of a tectonic earthquake refers to the orientation of the fault plane that slipped and allows for inferring the tectonic stress regime that caused the earthquake (Delvaux & Barth, 2010;

Table 1
Event and Preprocessing Parameters Provided by MQS (InSight Marsquake Service, 2020)

Source parameters	S0235b	S0173a	S0183a
Event quality	A	A	B
Back azimuth (°)	74	91	61
Epicentral distance (°)	25	29	~43
Origin date	July 26, 2019	May 23, 2019	June 3, 2019
Origin time (UTC)	12:16:15	02:19:33	02:22:17
P wave arrival (UTC)	12:19:19	02:22:59	02:27:45
S wave arrival (UTC)	12:22:06	02:25:54	02:32:09
Band-pass corner frequencies (Hz)	0.1–0.5	0.1–0.4	0.2–0.4

Michael, 1987; Molnar & Sykes, 1969). Focal mechanisms are derived from the polarity of arriving seismic waves and is usually involves combining records of multiple receivers. Single-station source inversion has always been a niche in terrestrial seismology, restricted to remote settings, where one particularly valuable seismic event was only recorded by one station or as an effort to do quick characterization of an event from a single record, before data of a full network could be easily collected and processed in bulk. This included mainly studies of normal modes (Buland & Gilbert, 1976; Ekström et al., 1986) or surface waves (Giardini et al., 1993, 1994; Jimenez et al., 1989). Single-station source inversion based on body waves has also been tried and shown to constrain the focal mechanism unambiguously if the SNR is high enough and the appropriate complete Green's function, i.e., the location of the event and the velocity structure in the region is known (Richards, 1978; Stump & Johnson, 1977). In modern observational seismology, source inversion is typically based on the polarity of first motion (Hardebeck & Shearer, 2002) to determine a focal mechanism. Inversion of the full moment tensor is usually based on the waveforms of surface waves (Ekström et al., 2012), body waves (Dziewoński et al., 1981; Vallée et al., 2011) or other phases such as the W phase, which is a very long-period phase (100–1,000s) (Duputel et al., 2012).

All these methods require data from a seismic network that recorded the event with a wide range of azimuths. In contrast, analyzing the InSight SEIS data requires going back to single-station approaches. Additionally, the absence of clear surface waves restricts our method to body wave arrivals only. We therefore had to adapt existing source inversion approaches to the InSight data.

Motivated by the location of the three Marsquakes S0235b, S0173a, and S0183a in areas suspected to be tectonically active beforehand (Figure 1) as well as the similarity of the LF events with tectonic events on Earth, we analyzed the three events under the assumption of a tectonic origin with the goal to resolve the spatial orientations of the fault planes at which the slip occurred. We developed an inversion strategy to resolve the moment tensors of the three events that honors the fact the InSight consists of a single three-component seismic station only. Because none of the event recordings of S0235b, S0173a, or S0183a exhibit clear surface waves or observable normal modes, we use the direct P and S body waves for events S0235b and S0173a, or only the P wave for event S0183a to determine the focal mechanism. We first present our MTI strategy encompassing the combination of a direct inversion of the waveforms for the moment tensor and an exhaustive grid search for all possible double-couple (DC) sources. We restrict our search to pure DC source mechanisms, i.e., forbid isotropic source components and interpret compensated linear vector dipole (CLVD) components as an indication of instability in the inversion. Pure DC sources indicate a tectonic origin. We assume the sources to be small enough in order to treat them as an instantaneous event on a fault smaller than the observed wavelengths. Independently, the two approaches indicate that both events S0235b and S0173a are governed by normal faulting. Because the focal mechanism associated with S0183a is inferred using only the P wave arrival, the determination of the focal mechanism for this event remains ambiguous but a normal fault character prevails.

2. Data

We analyze three high quality LF Marsquakes, S0235b, S0173a, and S0183a. The LF category of events show earthquake-like characteristics, which allows us to adapt methodologies that have been developed for application to earthquakes. The distance, back azimuth (BAZ) and location of the Marsquakes were estimated by the Marsquake Service (MQS) (InSight Marsquake Service, 2020) using the polarization of the P wave train and the time separation between P and S waves compared to a set of a priori velocity models (Böse et al., 2017; Clinton et al., 2018; Khan et al., 2016). The distance and BAZ for each event are listed in Table 1 and their location is specified in the caption of Figure 1. We use the continuous seismic records of the VBB instrument sampled at 20 Hz and rotate the seismograms into vertical (Z), radial (R), and transverse (T) components. The individual traces for the components and P and S waves are referred to as PZ, PR, PT, SZ, SR, ST hereinafter.

Figure 2 shows the raw recorded (Figures 2a–2c) and band-pass-filtered (Figures 2e–2g) vertical-component VBB data for events S0235b, S0173a, and S0183a. For comparison, we also display the recording of an intermediate depth, magnitude M_w 6.5 earthquake that occurred in Greece (January 6, 2008, 05:14:06 UTC) and was recorded in Switzerland at an epicentral distance of 1,500 km, similar to the Marsquakes
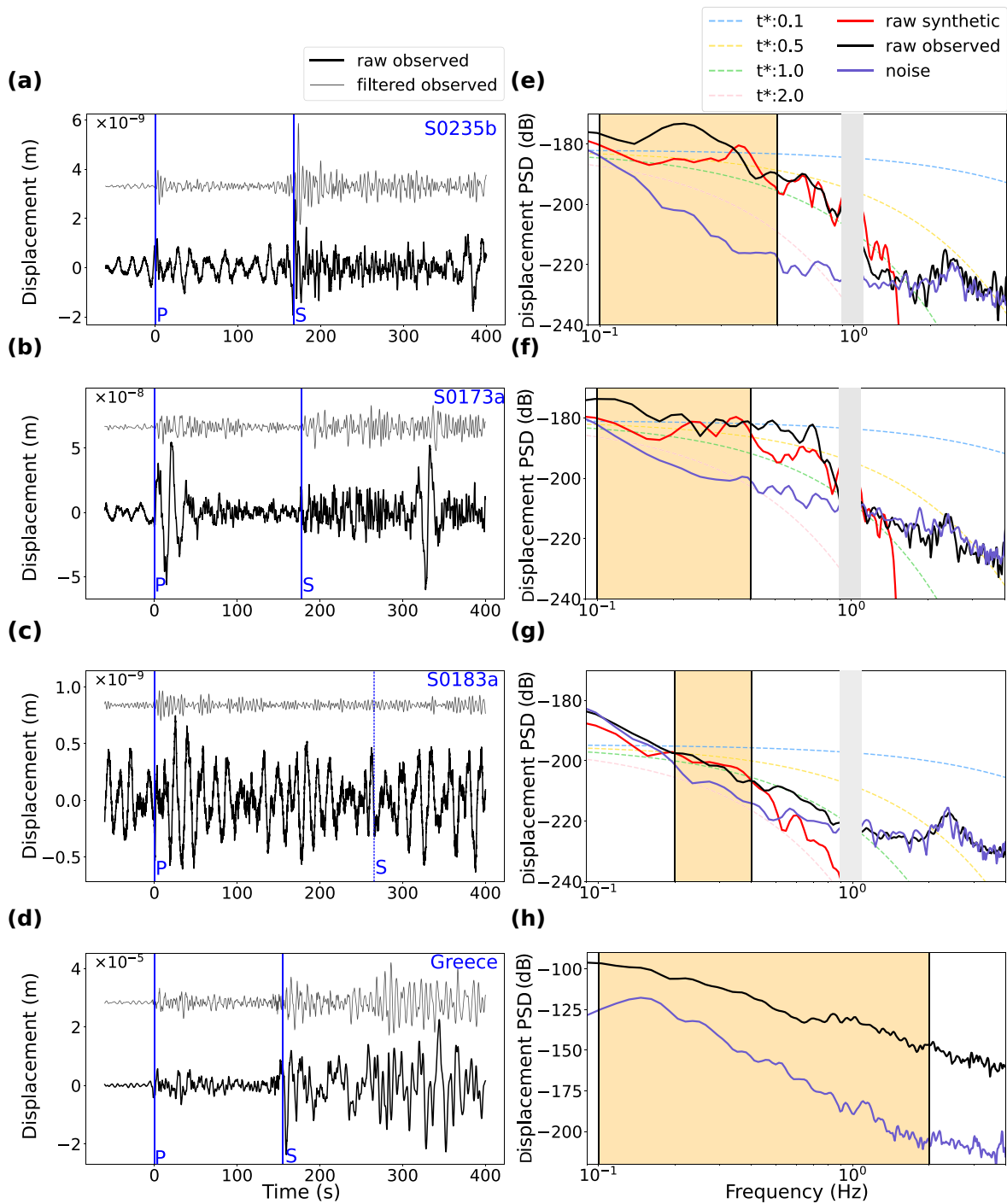
Figure 2. Raw and band-pass filtered vertical-component VBB data for the three Marsquakes that occurred on sols (a) 235, (b) 173, and (c) 183 (see Table 1 for event and preprocessing details). (d) Recording of an intermediate depth earthquake in a similar distance. The arrival times of the first arriving *P* and *S* waves are highlighted in blue. A dashed blue line is used to emphasize the weak S arrival of event S0183a. (e–h) Event spectra, preevent noise spectra and synthetic spectra are shown in black, purple and red, for all events, respectively. In (e–g), the gray box masks a 1-Hz electronic noise peak (Ceylan et al., 2020). The synthetic data are convolved with a *t** value such that synthetic and observed spectra match visually. Theoretical spectra for a number of *t** values are illustrated with the dashed lines in the background. The yellow shaded area represents the frequency band which is used in this study. VBB, very broadband.
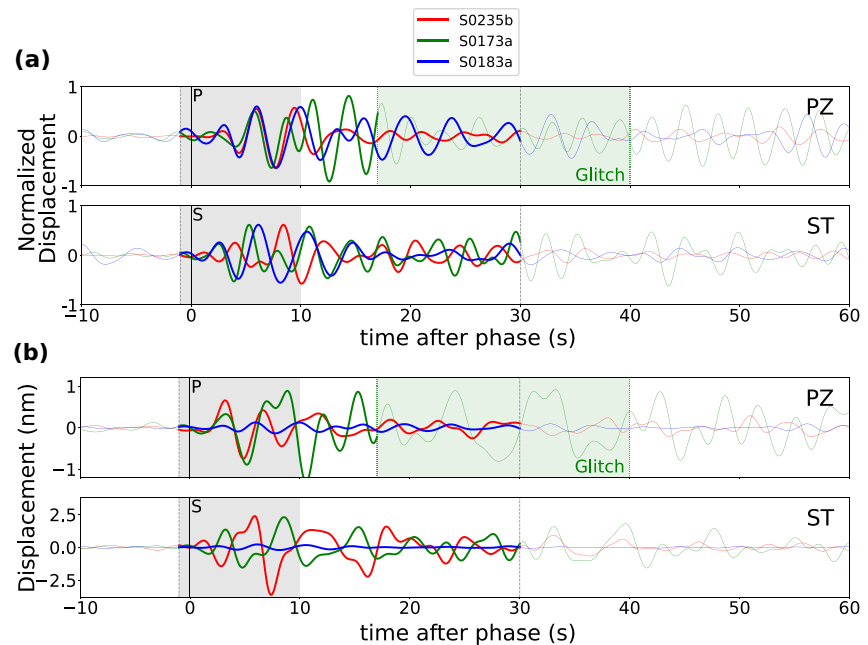
Figure 3. The recorded *P* waveform on the *Z* component (PZ) and *S* waveform on the T component (ST) for events S0235b, S0173a, and S0183a shown in blue, red and green, respectively. The gray dashed lines represent the start and end of the window used for our inversion methods, which is also emphasized with the bold colored waveforms. The black solid lines illustrate the onset of the *P* and *S* wave arrivals. The light-gray and green area represent the higher weighted part of the waveform and the glitch recording for event S0173a, respectively. (a) A common band-pass filter of 0.2–0.4 Hz applied to the data and each event is scaled to fit the maximum absolute amplitude of the first 10 s of event S0235b. (b) Nonscaled data passed through their individually selected band-pass filter specified in Table 1.

(Figures 2d and 2h). The waveforms are remarkably similar between the Martian and the terrestrial events, suggesting a tectonic origin of the three Marsquakes and a wave-propagation dominated by ballistic body waves with little scattering observed on lunar seismograms (Lognonné et al., 2020). While the waveforms are remarkably similar between the Martian and the terrestrial events, the observable bandwidth of the Marsquakes is much narrower. It only exceeds the preevent noise between 0.1 and slightly above 1 Hz. Since local three-dimensional structure, which we cannot expect to model correctly in our synthetic seismograms, starts to dominate at higher frequencies, we choose a narrower frequency band for analysis (Table 1). The seismograms are filtered with a nonzero-phase fourth order band-pass Butterworth filter.

We use data in a 31-s time window around each phase pick (*P* and *S*) on all components except the T component of the P phase (PT), which is excluded, because the back azimuth has been explicitly chosen to minimize *P* wave energy in the T component. This time window is chosen to contain the direct phases plus initial secondary arrivals (depth phases as well as reflections from the Moho and other internal boundaries). We shorten the time window of the *P* wave to 17 s for event S0173a, because the data is polluted by a strong glitch (Scholz et al., 2020). Glitches are artifacts of transient one-sided pulses often accompanied by high-frequency spikes and occur relatively frequently in the recorded VBB data. For all events, we observe an energy increase on the PT trace after 10–12 s, where receiver-side scattering starts to play a role. This scattering cannot be modeled by synthetic seismograms so far, due to the lack of a detailed local structural model. Therefore, we assign a lower weight to the time window from 10 to 30 s after the first arrival, but we do include this window to stabilize the inversion (see below).

Figure 3 shows the amplitude-normalized PZ and ST waveforms of the three Marsquakes. The first 10 s of the PZ waveforms show the same polarities for all three events. Yet, event S0235b shows a dissimilar polarity on ST waveforms for the first 10 s relative to events S0173a and S0183a. Therefore, we expect the fault regime of event S0235b to be distinct from the other two. The comparable initial polarities of the PZ and ST waveforms of events S0173a and S0183a indicate similar sources.
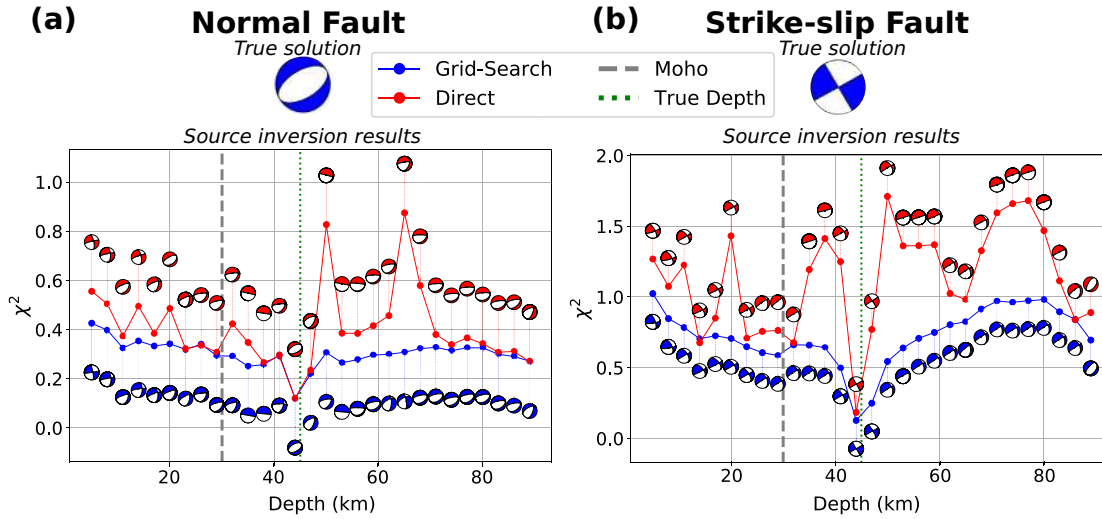
Figure 4. The inversion results of the synthetic event for the direct inversion (red) and GS method (blue) of (a) a normal fault system and (b) a strike-slip fault system both with a strike angle of 60°. The blue and red beachballs show the source solutions belonging to their misfit values (χ^2). The dashed gray line denotes the depth of the Moho and green dotted line illustrates the true depth location. GS, grid search.

3. Moment Tensor Inversion Strategy

We compare two approaches: a direct linear inversion for the full moment tensor and a grid search over all double-couple (DC) sources. For both our methods, we fix the location and origin time of the Marsquakes to the solution of the Marsquake service (MQS) (Table 1).

Both inversion methods rely on synthetic seismograms computed with AxiSEM (Nissen-Meyer et al., 2014) to a maximum frequency of 1 Hz and stored and accessed using an Instaseis database (van Driel et al., 2015). The background velocity model is purely elastic and radially symmetric. To simulate the effect of attenuation, the synthetic seismograms are convolved with a *t** operator, based on a chosen spectral decay function that matches the data (Figure 2). Our preferred velocity model, published as the TAYAK model in the InSight blind test (Clinton et al., 2017), consists of a mantle that is based on general assumptions of the bulk chemistry, mineralogy and areotherm (Khan & Connolly, 2008; Khan et al., 2018; Rivoldini et al., 2011). First observations on Mars showed that the TAYAK mantle profile is consistent with the nonobservation of an *S* wave shadow zone around 30° distance, but that the thick TAYAK crust (78 km) cannot explain receiver-side converted phases. We therefore recalculated the Instaseis database that consists of a two-layer crustal velocity profile that is compatible with initial receiver function (RF) analysis, with a Moho at 24 km depth (Lognonné et al., 2020) and an intracrustal interface at 10 km depth. Figure A1 shows both models. As it can be seen in Figures 4 and 6, a strong S-precursor is present on the radial component, which we generally fit well with this adapted crustal model. We use the RF-constrained velocity model as the preferred model, but tested our method with the original thick-crust model as well. We directly solve the linear inverse problem (hereinafter referred to as direct inversion) for the full deviatoric moment tensor as described in Minson and Dreger (2008), see Appendix B for details. This produces a full moment tensor with five free parameters, from which we select only the DC part for further analysis.

We define the misfit of each solution as

$$\chi^2 = \frac{1}{2}(\mathbf{d_{obs}} - \mathbf{d_{syn}})^T C_d^{-1}(\mathbf{d_{obs}} - \mathbf{d_{syn}}) \tag{1}$$

where $\mathbf{d_{obs}}$ and $\mathbf{d_{syn}}$ represent the selected part of the observed and synthetic waveform used for the inversion, respectively. The data covariance matrix C_d is a block-diagonal matrix with entries $(C_d)_{ii} = \frac{\sigma_i^2}{w_k}$, where σ_i^2 is the variance of trace i estimated in a 30-s time window before the phase arrival and w_k is a

phase-specific weighting factor that is 1 for the first 10 s and 1/10 for the rest of the trace. The value of 1/10 was empirically found to be a good compromise between stability and quality of fit. ST and PZ are considered to be the most robust under changing receiver site velocity structures, since converted receiver phases and precursors appear mainly on the SR, PR, and SZ. Therefore, we weighted SZ, SR and PR with an additional weighting factor of 1/10 to the entire trace.

We find that the direct inversion can result in high non-DC components of the moment tensor. To validate the DC solutions and explore its uncertainties, we additionally performed a grid search (GS) over the three unique orientation angles of the fault: strike, dip, and rake in 5° steps. For each step, the scalar moment of the corresponding source is estimated from a scaling factor between the observed and synthetic waveforms (Sigloch & Nolet, 2006):

$$M_0 = \frac{\mathbf{d}_{\mathrm{syn}}{}^T C_d \mathbf{d}_{\mathrm{obs}}}{\mathbf{d}_{\mathrm{syn}}{}^T C_d \mathbf{d}_{\mathrm{syn}}} \tag{2}$$

We choose only PZ and ST to estimate M_0 as they should represent the P and S wave arrivals most clearly. Once the synthetic data is rescaled by the estimated M_0 we calculate the misfit between the observed and synthetic data using Equation 1 for each grid point in the GS.

To understand the impact of the hypocenter depth on both algorithms, we vary it from 5 to 89 km in 3 km steps. For each depth step, we store the single optimal source solution calculated by the direct inversion. For the grid search, we present all focal mechanisms with a misfit difference of less than 5% to the lowest misfit found. This allows us to compare the various source solutions determined from both methods as a function of depth.

In order to compare the source solutions of both algorithms, we use the misfits in DC model space. The full moment tensor solutions obtained from the direct inversion (m_{xx}, m_{yy}, m_{zz}, m_{xy}, m_{xz}, m_{yz}) are therefore converted into the nonunique DC model space (strike, dip, rake, and scalar moment). The nonunique conversion results in two possible source solutions, i.e., the fault and auxiliary plane solutions. Focal mechanism solutions in the DC domain are not only nonunique, but also distributed in a spherical model space (Tape & Tape, 2012). These two characteristics induce complexity when computing statistical moments (such as the variance). Therefore, instead of computing the statistical moments we illustrate the uncertainties by showing the one-dimensional posterior marginals of the strike, dip, and rake. Additionally, we plot the focal mechanisms in the form of probabilistic beachballs, i.e., superpositions of all acceptable focal mechanisms (Stähler & Sigloch, 2014). Additionally, we convert the GS solutions for all depths with $\epsilon < 0.2$ into the full moment tensor component basis (i.e., m_{xx}, m_{yy}, etc.) to calculate the mean. Subsequently, we convert the mean back into the DC model space and present it together with its complementary solution (either the fault or auxiliary plane solution) and the mean scalar moment.

4. Implementation

We test the performance of the direct inversion and GS method on events created synthetically with real Martian noise added to the seismograms. Simultaneously, we acquire information about the effect of e.g., noise, window length, weight factors, arrival times and band-pass filters on the inferred source solutions. Here, we present an example of such a test by showing the inversion results of two synthetic events with different fault regimes (a strike-slip and a normal fault) with real Martian noise added to the seismograms. We choose a synthetic event rather than an earthquake, because important tuning parameters (e.g., the frequency range of band-pass filters) for Mars and Earth events are dissimilar. An example to this is shown in Figure 2, where the event spectra of the earthquake in Greece exceeds the noise spectra for a much broader frequency band than the event spectra of the Marsquakes.

The synthetic test events are located close to the location of event S0235b (11°N/170°E) with a source depth of 45 km. The magnitude is $M_w = 3.1$. The location of the recording station is identical to InSight lander. The velocity model used to create this synthetic event corresponds to the RF-derived velocity model, see Figure A1. To simulate real data, we added noise to the synthetic seismograms, that corresponds to actual
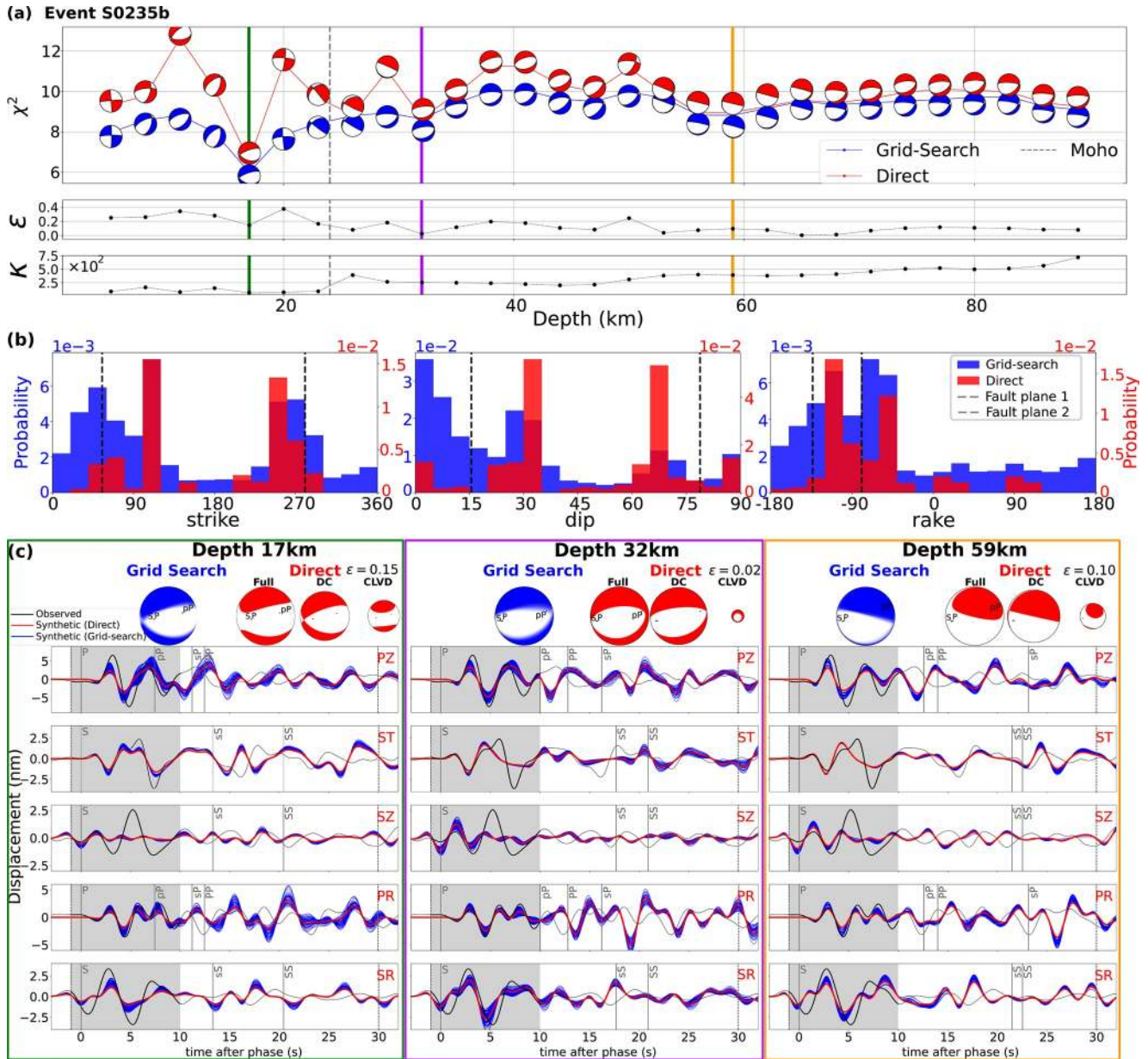
Figure 5. Inversion results for event S0235b for the RF-constrained velocity model. (a) The misfit (χ^2), CLVD/DC ratio (ε) and the condition number (κ) are plotted as a function of depth (dashed gray line: Moho depth). The blue and red beachballs show source solutions for the lowest χ^2 of the GS and direct inversion, respectively. The colored lines correspond to the detailed results in (c). (b) The strike, dip and rake distributions, weighted by the exponential negative misfit value, in the DC model space for solutions at all depths with $\varepsilon < 0.2$ for the GS and direct inversions in blue and red, respectively. The dashed gray lines show the mean solution, computed in the full moment tensor component basis, and its complementary solution (see Tables 2 and C1 for the mean solutions in DC model space and full moment tensor component basis, respectively). (c) The solutions of the GS (blue) and direct inversion (red) at 17 (green box), 32 (purple box) and 59 (yellow box) km depth, the latter split into DC and CLVD (scaled by their M_0). The probabilistic beachball from the grid search shows solutions of the 5% lowest misfit values. The ray piercing-points of P, S, and pP are indicated by the black dots in the beachballs. The five waveform windows represent the data compared to the best fits for all methods, the gray shaded area marks the stronger weighted part of inversion window. The solid gray vertical lines denote theoretical arrival times for direct and depth phases. CLVD, compensated linear vector dipole; DC, double-couple; GS, grid search.

Martian noise recorded with the VBB for an hour of relatively glitch-free noise of comparable amplitude to what has been observed during event S0235b.

The two synthetic events have different source types: a normal (Figure 4a) and a strike-slip fault (Figure 4b), both with a strike angle of 60°, i.e., pointing toward the receiver. The lowest misfit for both synthetic events

Table 2
The Moment Tensor Solutions in DC Model Space and the Magnitude Estimate for Events S0235b, S0173a, and S0183a

	S0235b	S0173a	S0183a
	FP 1 (FP 2)	FP 1 (FP 2)	FP 1 (FP 2)
Moment tensor			
Strike (°)	280 (55)	55 (320)	58 (322)
Dip (°)	79 (15)	88 (15)	86 (37)
Rake (°)	−79 (−134)	−105 (−6)	−126 (−7)
Magnitude			
M_0 (10^{12} Nm)	52 ± 8	41 ± 11	55 ± 41
M_w	3.1	3.0	3.1

Note. The solutions represent the mean and its complementary solution of the GS results for a CLVD/DC ratio (ε) < 0.2 computed in full moment tensor component basis (see Table C1 for the full moment tensor components). These two no-unique solutions, the fault or auxiliary plane solution, are referred to as fault plane (FP) 1 and 2.

is found at the true source depth and the corresponding moment tensors are representing the true solution. The moment tensor solutions closest to the true solution are characterized by relatively low ε, i.e., stable source solutions. The results of these tests show that we are able to identify the correct mechanism using a single station in the presence of noise, albeit not modeling errors.

Since we are looking for tectonic events, we consider the estimated compensated linear vector dipole (CLVD) component as a measure of stability, i.e., source solutions with a high CLVD component correspond to unstable solutions. Additionally, the stability of the inversion with respect to noise can be estimated by the condition number κ of the inverse problem (Equation B3), defined as the ratio of the largest to smallest eigenvalue of $G^T C_d G$ (Lanczos, 1996). The condition number represents the sensitivity of the inferred solutions to uncertainties in the data (e.g., caused by noise) and therefore tells us if the inverse problem is able to recover the source solution. Large κ indicate less stable source solution (Stump & Johnson, 1977). We generally notice that κ increases for larger depths, because secondary phases, specifically surface-reflected depth phases are moving out of the time window used for inversion.

5. Results

In the following, we present the estimated source solutions for both the GS and direct inversion for various depths of the three Marsquakes. For each solution, we also show the measure of stability of the obtained source solutions represented by the CLVD/DC ratio (ε) and the condition number (κ). For events S0235b and S0173a, we select three depth ranges for further investigation, including also a preferred range, where ε is relatively low and where calculated depth phase arrivals (e.g., pP and sS) from ray theory seem to match unidentified phase arrivals of the observed recordings. For event S0183a we show the inferred source solutions and corresponding waveforms obtained from the GS. We do not present the solutions obtained from the direct inversion for this particular event because of the nonunique solution.

5.1. S0235b

Inversion results for event S0235b for the RF-derived velocity model are shown in Figure 5. In Figure 5a, we show the trend in misfit, ε and κ as a function of depth. Figure 5b shows the strike, dip and rake distributions for all possible depths with ε < 0.2, weighted by probability, compared to the fault planes of the direct inversion results. The mean solutions are determined from the GS solutions in full moment tensor component basis (see Table C1) and subsequently converted back into the DC model space (see Table 2 and Figure 5b).

The direct inversion results in a solution that is mostly DC (ε < 0.2 for depths below the Moho) and consequently, the GS and direct inversion produce similar focal mechanisms, of normal fault style for most proposed depths. The focal mechanisms are relatively well-constrained as normal faulting, with the strike mainly oriented E-W (~280°) and the rake around ~ −79° (see Figure 5b and Table 2). In contrast, the distributions for the dip angle are much broader and it is the least constrained component of the obtained source solutions. For the three selected depth ranges, the dip angle increases with depth and the rake angle varies slightly.

Figure 5c shows the fit of synthetic waveforms for three depths of interest. All solutions fit the polarity of the first motion of PZ, ST, PR, and SR. The precursor on SR and SZ is fit well in terms of arrival time, showing the power of the adapted crustal velocity model, although the amplitude fit on SZ is relatively poor. The relative amplitudes of the first 5 s of PZ, ST, and SR match predicted phases, but there are secondary phases around 10 s (PZ), 7 s (ST), and 5 s (SZ), which are not fit at all for the deeper sources. The 17 km source fits this peak with pP and a intracrustal reverberation respectively, however, both of these phases are highly sensitive to the exact source and velocity model, leading to the high scatter in proposed focal mechanisms around 17 km, while the local misfit minima at 32 and 59 km are much more stable. Figure 6 compares

synthetic waveforms and ray-theoretical travel times with the actual data for a wider depth range. It shows that these secondary arrivals could only be matched as depth phases for hypocenters around 15–20 km depth. At these depths, just above the presumed Moho, the dependency of the waveform on the source-side velocity structure is specially high, as is visible in the rapidly changing focal mechanisms in Figure 5a. More stable solutions are found around 30–35 and 55–65 km depth.

The estimated scalar moment ($M_0 = 5.2 \times 10^{13}$ Nm, $M_W = 3.1$) is lower than the spectral magnitude estimate of $M_{FB}^{Ma} = 3.6$ in Giardini et al. (2020).
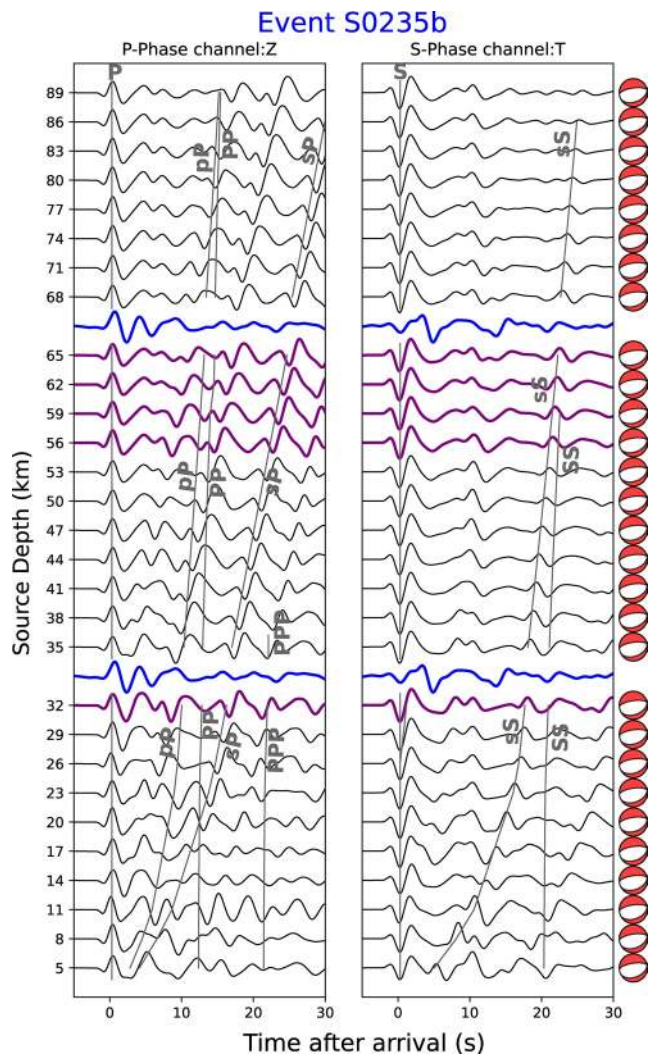

Figure 6. Synthetic seismograms (black lines) generated for the RF-derived velocity model with the source solution shown on the right at depths ranging from 5 to 89 km in 3 km steps. The left and right figure show the *P* wave on the vertical component and the *S* wave on the transverse component, respectively. Predicted arrival times of the direct, depth and secondary phases (P, S, pP, sP, sS, PP, PPP, SS), are shown by the gray labeled lines. The direct phase arrival times are shifted to the peak arrival rather than the onset. For easier comparison, the observed data (blue) is plot twice. The purple seismograms correspond to our preferred source depths. All seismograms are filtered from 0.1–0.5 Hz individually normalized. RF, receiver function.

5.2. S0173a

Inversion results for event S0173a are shown in Figure 7, in the same layout as Figure 5. A general result is that the CLVD component is higher for most proposed depths compared to S0235b and as a result, the DC component of the direct inversion diverges from the result of the grid search for many depths (Figure 7a). We find lowest misfits at 14 km depth, but with low stability with respect to depth changes, and considerably more stable solutions around 35–40 and 60 km hypocentral depth. The strike is mainly oriented NE-SW (~55°) and the rake describes both a normal fault (~ −105°) and a strike-slip (~ −6°) regime (Figure 7b). The dip angle is poorly constrained, specifically for the direct inversion, while the distribution of the GS shows tendency to a steep dip angle. The general normal faulting style with higher obliqueness is the result of the matching initial polarity and relative amplitude of PZ, ST, and SR (Figure 7c). It has been observed that the amplitude ratio of PZ and PR is difficult to fit, hinting at unmodelled shallow structure at the receiver. As in the case of S0235b, the observed phase on ST arriving at ~8 s does not match the synthetic waveforms.

For identification of later arrivals, we compare in Figure 8 the observed data with predicted phase arrivals from ray theory and synthetic waveforms. For example, the big arrivals ~10 s after the *P* wave arrival and ~18 s after the *S* wave arrival on the observed data can be well explained by the pP and sS arrivals, respectively, if a depth around 35 km is chosen. It also demonstrates that a more detailed source-side crustal model is necessary to consolidate depth results.

The estimated scalar moment ($M_0 = 4.1 \times 10^{13}$ Nm, $M_W = 3.0$) is again significantly lower than the MQS spectral magnitude estimate of $M_{FB}^{Ma} = 3.7$, but compatible with the body wave magnitude $m_{b,P} = 3.3$ Giardini et al. (2020).

5.3. S0183a

Event S0183a has a small *S* wave amplitude, which has been interpreted as a result of a *S* wave low velocity zone in the lithosphere (Giardini et al., 2020; Smrekar et al., 2019). The available structural models are not able to reproduce such a weak *S* wave signal given the estimated source location. Therefore, we invert only *P* waves for this event to determine the source solution. We did not perform a direct inversion for this event, which would have been highly unstable with only one *P* wave. The inversion results of the GS for event S0183a for the RF-constrained velocity model are shown in Figure 9. The source solutions corresponding to the lowest misfit at various depths are highly varying (see Figure 9a). As it can be expected from the similarity in *P* waveforms with the other events
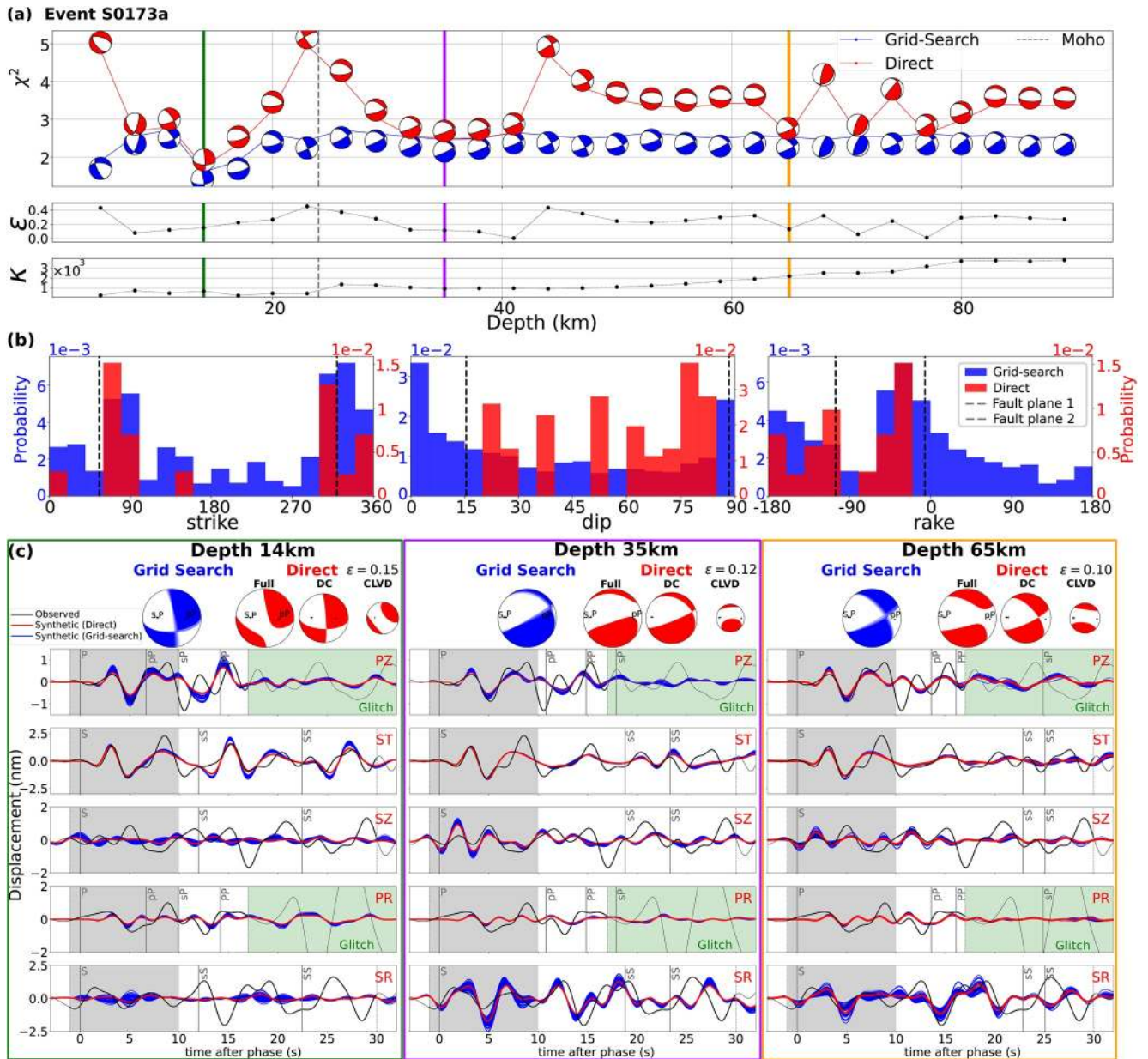
Figure 7. Inversion results for event S0173a for the RF-constrained velocity model. (a) The misfit (χ^2), CLVD/DC ratio (ε) and the condition number (κ) are plotted as a function of depth (dashed gray line: Moho depth). The blue and red beachballs show source solutions for the lowest χ^2 of the GS and direct inversion, respectively. The colored lines correspond to the detailed results in (c). (b) The strike, dip and rake distributions, weighted by the exponential negative misfit value, in the DC model space for solutions at all depths with $\varepsilon < 0.2$ for the GS and direct inversions in blue and red, respectively. The dashed gray lines show the mean solution, computed in the full moment tensor component basis, and its complementary solution (see Table 2 and C1 for the mean solutions in DC model space and full moment tensor component basis, respectively). (c) The solutions of the GS (blue) and direct inversion (red) at 14 (green box), 35 (purple box), and 65 (yellow box) km depth, the latter split into DC and CLVD (scaled by their M_0). The probabilistic beachball from the grid search shows solutions of the 5% lowest misfit values. The ray piercing-points of P, S, and pP are indicated by the black dots in the beachballs. The five waveform windows represent the data compared to the best fits for all methods, the gray shaded area marks the stronger weighted part of inversion window. The solid gray vertical lines denote theoretical arrival times for direct and depth phases. CLVD, compensated linear vector dipole; DC, double-couple; GS, grid search; RF, receiver function.

(see Figure 3a), the distributions shown in Figure 9b show similar distributions to event S0173a, of normal fault character with obliqueness. The mean of the strike is around 55° (see Table 2), but the dip angle is mostly unconstrained. The scalar moment is estimated around 10^{14} Nm, or $M_W = 3.3$, higher than the MQS estimate of 2.9.
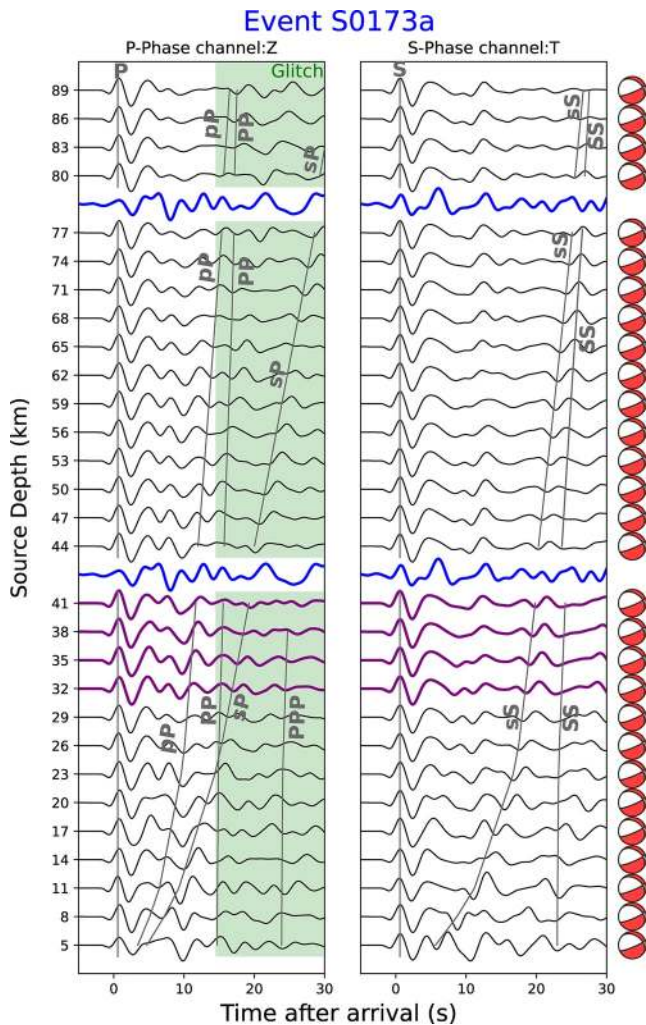
Figure 8. Synthetic seismograms (black lines) generated for the RF-derived velocity model with the source solution shown on the right at depths ranging from 5 to 89 km in 3 km steps. The left and right figure show the *P* wave on the vertical component and the *S* wave on the transverse component, respectively. Predicted arrival times of the direct, depth and secondary phases (P, S, pP, sP, sS, PP, PPP, SS), are shown by the gray labeled lines. The direct phase arrival times are shifted to the peak arrival rather than the onset. For easier comparison, the observed data (blue) is plot twice. The purple seismograms correspond to our preferred source depths. All seismograms are filtered from 0.1 to 0.4 Hz individually normalized. The green shaded area marks the time range perturbed by a glitch. RF, receiver function.

6. Discussion

The results for three Marsquakes with high SNR body waves show that it is possible to constrain focal mechanisms from single-station recordings. Nevertheless, a number of caveats remain.

Most prominently, we found lowest misfits for hypocenters above the Moho (at 24 km depth) for the RF-constrained velocity model, where secondary arrivals around 8 s after the direct P phase are explained as pP depth phases. However, these misfit minima are typically constrained to exactly one depth. A slight change to this depth causes a major change in the preferred focal mechanism, since the depth phase arrival is moving in time. Solutions below the Moho, between 30 and 40 km depth are more stable in focal mechanism with respect to depth changes. The secondary peaks are then explained as underside reflections from the Moho or an intracrustal interface at the source side. Additionally, the presence of a strong intracrustal interface is necessary to explain the S-precursors and the converted phases in the P coda, as shown by preliminary receiver function results (Lognonné et al., 2020). Figures D1 and D2 show the effect of depth on expected arrival times of underside reflected and refracted phases. For the time being, it is not possible to confirm one or the other depth. Despite the lower misfit values, we are hesitant to prefer the shallower depth for the following reasons:

- The source inversion is considerably less stable if the source is placed between the Moho and the intracrustal discontinuity, since small variations in depth or the velocity structure move peaks in the coda substantially. This increases the chance of spurious fitting, which we want to avoid
- For none of the events, clear surface waves are observed. We cannot expect to observe event signal below 0.1 Hz due to the instrument noise (Figure 2). However, high-frequency fundamental mode surface waves are also not observed, which can be explained by dispersion (the event depth is larger than the penetration depth). For example, the penetration depth for 10 s surface waves with a Rayleigh wave group velocity of 3 km/s is around 15 km, suggesting a source at least this deep
- Due to the lower thermal gradient of Mars the seismogenic depth is larger, compared to Earth, and there is no a priori reason to assume that intraplate seismicity is restricted to shallow, intracrustal depths (Plesa et al., 2018)

We therefore conclude that the existence of stable solutions for focal mechanisms below the Moho, between 33 and 40 km depths is an encouraging first result that can be refined once a community model of the Martian crust has been established.

Furthermore, less stable focal mechanism solutions and less well-matching waveforms throughout the full depth range are found when inverting with the premission model TAYAK that has a much thicker crust of 78 km (Figure E1). The SZ at ~7 s is better fit for the TAYAK model (Figure E1b) compared to Figure 5c, whereas the SR fits are worse in the case of the TAYAK model. Specifically, the precursor to the radial component of the *S* wave and the *P* wave coda cannot be fit without a relatively shallow Moho. Premission estimates from gravity maps suggest that the Moho is about 30% deeper in the Cerberus Fossae region compared to the InSight landing site. Since our synthetic seismograms are computed in a spherically symmetric planet with constant interface depth, this effect is not considered.

Another effect that is not completely understood yet, is the frequency content of the seismic sources. We find that we can explain the spectra well with pure attenuation effects and t^* values of around 1 s, which is
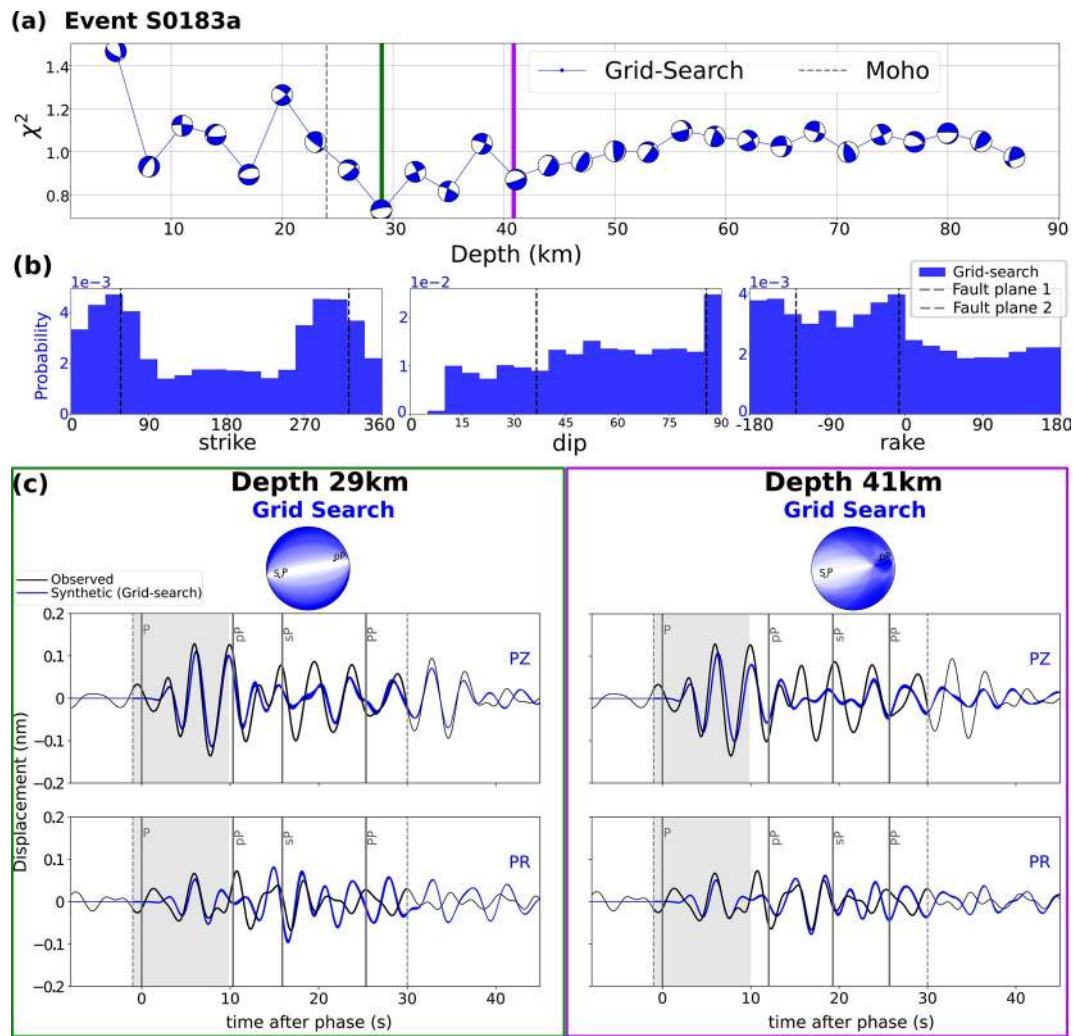
Figure 9. Inversion results for event S0183a for the RF-constrained velocity model. The S waves are not included, since they were not clearly observed for this event. Consequently, the direct inversion is not shown for this event. (a) The misfit (χ^2) is plotted as a function of depth (dashed gray line: Moho depth). The blue beachballs show source solutions for the lowest χ^2 of the GS. The colored lines correspond to the detailed results in (c). (b) The strike, dip, and rake distributions, weighted by the exponential negative misfit value, in the DC model space for solutions at all depths for the GS in blue. The dashed gray lines show the mean solution, computed in the full moment tensor component basis, and its complementary solution (see Table 2 and C1 for the mean solutions in DC model space and full moment tensor component basis, respectively). (c) The solutions of the GS (blue) at 29 (green box) and 41 (purple box) km depth. The probabilistic beachball from the grid search shows solutions of the 5% lowest misfit values. The ray piercing-points of P, S, and pP are indicated by the black dots in the beachballs. The two waveform windows represent the data compared to the best fits for all methods, the gray shaded area marks the stronger weighted part of inversion window. The solid gray vertical lines denote theoretical arrival times for direct and depth phases. DC, double-couple; GS, grid search; RF, receiver function.

relatively low, compared to teleseismic events on Earth. This also limits the source durations to less than a second. Estimations of stress drop or fault size based on source time functions would first require a better Q model of the lithosphere, an ongoing effort in the InSight project.

Finally, a discrepancy up to 0.6 (S0173a) is observed between magnitude estimates from this study and the magnitudes from Böse et al. (2018) and Giardini et al. (2020) (Table 3). The latter two studies used three magnitude estimates: a spectral magnitude M_{FB} from the low-frequency spectral plateau amplitude of the S wave train, and two separate body wave amplitudes m_b, $m_{b,S}$ for P and S waves, respectively. For S0173a and S0235b, the spectral magnitude estimate and the S wave magnitude $m_{b,S}$ are higher than our estimates, while the P wave magnitude m_b for event S0235b is matching better. This is most likely an effect of the radiation pattern, which leads to relatively high S wave amplitudes for this event, resulting in an over-prediction of the S wave based magnitudes M_{FB} and $m_{b,S}$. This is in the end an artifact due to the orientation of Cerberus Fossae with respect to the InSight lander, but has implications for estimating the seismic moment

Table 3
Moment Magnitude Estimates From This Study Compared to Previous Magnitudes From Giardini et al. (2020)

Event	M_W (this study)	M_{FB}	m_b	$m_{b,S}$
S0235b	3.1	3.6	3.2	3.6
S0173a	3.0	3.6	3.6	3.5
S0183a	3.3	3.1	3.3	3.2

Note. Our magnitudes for S0235b and S0173a are in reasonable agreement with the *P* wave based body wave magnitude $m_{b,P}$.

release of the region and of Mars as a whole. The magnitude scale used in Giardini et al. (2020) is currently in revision for future releases of the MQS event catalog, taking the results of this study into account.

7. Conclusion and Outlook

In this work, we find that two LF Marsquakes (S0235b and S0173a), located in Cerberus Fossae are likely the result of normal faulting with a relatively steep dipping fault plane, suggesting a predominantly extensive tectonic regime mainly oriented E-W to NE-SW. In the source region Orcus Patera, where event S0183a has been located, uncertainty in determining the fault regime is larger, yet the similar P-polarity compared to the other events suggests a similar, normal faulting regime in this enigmatic region.

Since source depths are not constrained yet, it remains unclear whether surface expressions can be directly related to the observed Marsquakes, but the overall match in strike direction is encouraging.

This study provides a first glance at tectonic mechanisms on another planetary body than the Earth. It will be extended to more Marsquakes, which have not been located so far to constrain whether extensional faulting is the dominant style on the whole planet. Once a global crustal model is available, more detailed coda modeling will help constrain the depth of Marsquakes and unlock an understanding of tectonic mechanisms in the crust of a single-plate planet.

The results of this study will be included in future releases of the Marsquake Service event catalog Clinton et al. (2021)

Appendix A: Velocity Models

Here, we illustrate the structural velocity models that we used to infer the source solution of the Marsquakes (Figure A1). The TAYAK model (red) is only based on premission estimates (Clinton et al., 2017), and was updated for this study based on preliminary receiver function results of the InSight mission (Lognonné et al., 2020).
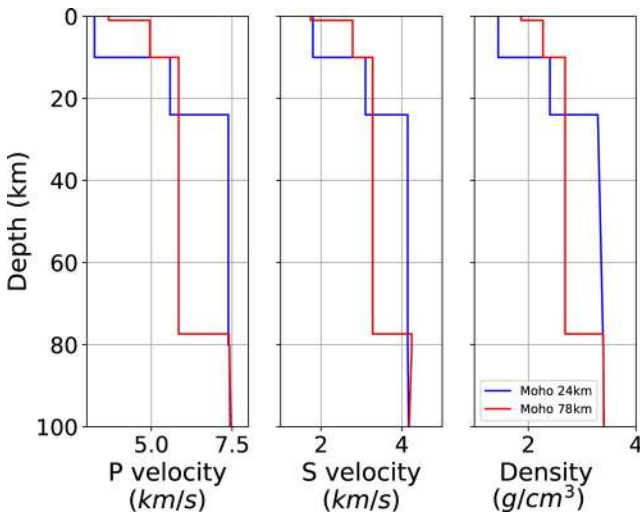

Figure A1. The *P* and *S* velocity and density of the first 100 km are illustrated for the RF-constrained velocity model and the TAYAK-premission model in blue and red, respectively. The RF-constrained velocity model includes upper-velocity layering information based on estimated receiver functions (Lognonné et al., 2020). RF, receiver function.

Appendix B: Linear Source Inversion

Our direct inversion method solves the inverse problem of seismic sources using a linear time domain moment tensor inversion. We use the north-east-down (NED) coordinate system convention with north (x), east (y) and down (z) according to Aki and Richards (2002):

$$\mathbf{d_{obs}} = G\mathbf{m} \tag{B1}$$

where G and $\mathbf{m}$ represent the Green's function matrix and a vector representation of the moment tensor components, respectively. We use Equations 6–8 from Minson and Dreger (2008) to define our Green's function:

$$
\begin{aligned}
\mathbf{u_z} = {} & m_{xx}\left[\frac{\mathbf{ss_z}}{2}\cos(2az) - \frac{\mathbf{dd_z}}{6} + \frac{\mathbf{ep_z}}{3}\right] \\
& + m_{yy}\left[-\frac{\mathbf{ss_z}}{2}\cos(2az) - \frac{\mathbf{dd_z}}{6} + \frac{\mathbf{ep_z}}{3}\right] \\
& + m_{zz}\left[\frac{\mathbf{dd_z}}{3} + \frac{\mathbf{ep_z}}{3}\right] \\
& + m_{xy}[\mathbf{ss_z}\sin(2az)] \\
& + m_{xz}[\mathbf{ds_z}\cos(az)] \\
& + m_{yz}[\mathbf{ds_z}\sin(az)]
\end{aligned}
\tag{B2}
$$

$$\mathbf{u_r} = m_{xx}\left[\frac{\mathbf{ss_r}}{2}\cos(2az) - \frac{\mathbf{dd_r}}{6} + \frac{\mathbf{ep_r}}{3}\right]$$
$$+ m_{yy}\left[-\frac{\mathbf{ss_r}}{2}\cos(2az) - \frac{\mathbf{dd_r}}{6} + \frac{\mathbf{ep_r}}{3}\right]$$
$$+ m_{zz}\left[\frac{\mathbf{dd_r}}{3} + \frac{\mathbf{ep_r}}{3}\right]$$
$$+ m_{xy}[\mathbf{ss_r}\sin(2az)]$$
$$+ m_{xz}[\mathbf{ds_r}\cos(az)]$$
$$+ m_{yz}[\mathbf{ds_r}\sin(az)]$$
$$\mathbf{u_t} = M_{xx}\left[\frac{\mathbf{ss_t}}{2}\sin(2az)\right]$$
$$+ m_{yy}\left[-\frac{\mathbf{ss_t}}{2}\sin(2az)\right]$$
$$+ m_{xy}[-\mathbf{ss_t}\cos(2az)]$$
$$+ m_{xz}[\mathbf{ds_t}\sin(az)]$$
$$+ m_{yz}[-\mathbf{ds_t}\cos(az)]$$

where u is the surface displacement, az is the azimuth, ss is the vertical strike-slip Green's function, ds is the vertical dip-slip Green's function, dd is the 45° dip-slip Green's function and ep is the explosion Green's function. z, r, and t refer to the vertical, radial and tangential components, respectively. m_{xx}, m_{yy}, m_{xy}, m_{xz}, m_{yz} represent the five-independent components of the moment tensor. The isotropic component of the moment tensor is assumed to be zero, which allows us to express the moment tensor in terms of five-independent components.

We can compute a generalized inverse using a concatenated version of the five data windows and their corresponding fundamental Green's function to estimate the individual moment tensor components:

$$\mathbf{m_{est}} = (G^T C_d G)^{-1} G^T C_d \mathbf{d_{obs}} \tag{B3}$$

where $\mathbf{m_{est}} = \left[m_{xx}, m_{yy}, m_{xy}, m_{xz}, m_{yz}\right]^T$. C_d is the data covariance matrix that incorporates the data uncertainty (i.e., standard deviation), σ, of a 30-s window before the phase arrival on each component. Because each trace has an individual σ value, the covariance matrix is a block-diagonal matrix constructed from five individual unit matrices multiplied with the appropriate constant. As mentioned in the main text, we apply more weight to the first 10 s of the data (i.e., 200 samples) using a weighting factor w (see main text for the values of w). Thus, C_d is given by

$$C_d(k + i \times nt, k + i \times nt) = \frac{\sigma_i^2}{w_k} \tag{B4}$$

where k represents the current sample, i refers to the number of the current window (e.g., $i = 0$ for PZ) and nt is equal to the total amount of samples within the current window.

Finally, we decompose the moment tensor into its double-couple (DC) and compensated linear vector dipole (CLVD) component following Jost and Herrmann (1989). We had already constrained the isotropic component to be zero. The deviatoric part of the moment tensor is then split into the DC and CLVD components expressed in terms of the eigenvectors and eigenvalues. The ratio between the smallest (in absolute sense) and the maximum eigenvalue $|e_{min}|$ and e_{max}, respectively, is the ratio of the DC component and the CLVD component:

$$\epsilon = \frac{|e_{min}|}{e_{max}}. \tag{B5}$$

Appendix C: Solutions in Full Moment Tensor Parameterization

Table C1 shows the moment tensor solutions for events S0235b, S0173a, and S0183a in expressed in the full parameterization (i.e., five-independent components). These solutions represent the mean of either the GS or direct inversion for $\epsilon < 0.2$, weighted by the negative exponent of the misfit. Each depth that is selected (i.e., depths with $\epsilon < 0.2$) contains of one solution for the direct inversion and multiple solutions (5% of the lowest misfit values) for the GS. The GS solutions of Table C1 are converted into the DC model space and shown in Table 2. The resulting uncertainties per parameter are relatively large, but this does not take into account their high correlation. The overall source uncertainty is therefore better expressed qualitatively in the probabilistic beachball plots.

Table C1
The Moment Tensor Solutions In The Full Parameterization for Events S0235b, S0173a, and S0183a

Moment tensor	S0235b		S0173a		S0183a
	Grid search	Direct	Grid search	Direct	Grid search
m_{xx} ($\times 10^{12}$ Nm)	-1.0 ± 3.0	-0.63 ± 2.6	-3.3 ± 6.2	-3.5 ± 5.2	-14 ± 23
m_{yy} ($\times 10^{12}$ Nm)	14 ± 15	19 ± 15	7.0 ± 9.6	13 ± 9.8	18 ± 31
m_{zz} ($\times 10^{12}$ Nm)	-13 ± 15	-19 ± 15	-3.8 ± 7.6	-9.6 ± 5.0	-2.8 ± 32
m_{xy} ($\times 10^{12}$ Nm)	-3.9 ± 5.6	-2.8 ± 4.8	5.8 ± 6.4	7.4 ± 4.9	5.3 ± 56
m_{xz} ($\times 10^{12}$ Nm)	30 ± 13	22 ± 11	-19 ± 15	-15 ± 12	-19 ± 79
m_{yz} ($\times 10^{12}$ Nm)	6.6 ± 10	-0.9 ± 9.0	16 ± 6.8	12 ± 3.0	13 ± 17

Note. The solutions represent the mean of the GS and direct inversion results for all depths with CLVD/DC ratio $(\epsilon) < 0.2$.

Appendix D: Phase Tracking

Figure D1 shows predicted arrivals of underside reflections, conversion phases, depth phases, and secondary phases for the RF-constrained velocity model on the PZ component for event S0173a and S0235b calculated using ray theory. These velocity phases arrive within approximately 10 s after the *P* arrival. For example, the P10s phase, a *P* wave converting to an *S* wave at the 10 km interface, matches the trough around 3 s after the *P* wave arrival for both events. Also, the P24s, a *P* wave converting to an *S* wave at the Moho, could potentially explain the peak arriving right after that trough.

Appendix E: Results for the TAYAK-Premission Model

Figures E1 and E2 show the inversion results using the the TAYAK-premission model for event S0235b and S0173a, respectively. We find that in particular ϵ increases with respect to the solutions obtained for the RF-constrained velocity model. This results in source solutions with a relatively low DC component, which is considered to be unstable. The waveform fits from the GS are substantially better than the direct inversion due to an underestimated scalar moment for the direct inversions and thus amplitude mismatches with the observed data.
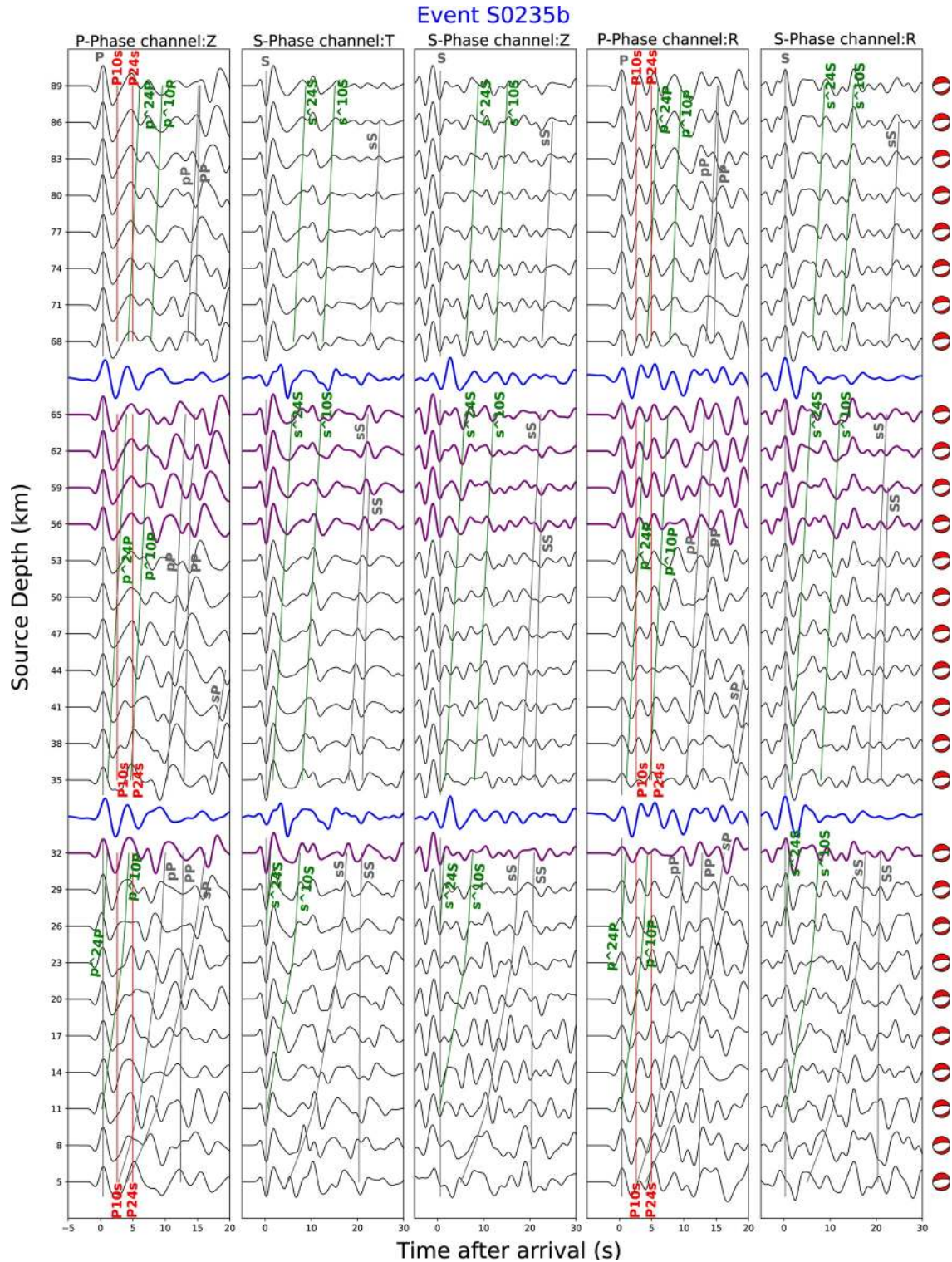
Figure D1. Synthetic seismograms (black lines) generated for the RF-constrained velocity model with the source solution shown on the right at depths ranging from 5 to 89 km in 3 km steps. From left to right the plots show the *P* wave on the vertical component (PZ), the *S* wave on the transverse component (ST), the *S* wave on the vertical component (SZ), the *P* wave on the radial component (PR) and the *S* wave on the radial component. The arrival times of the direct, depth, secondary phases (P, S, pP, sP, sS, PP, PPP, SS), based on ray theory, are shown by the gray labeled lines. The red and green labeled lines show the calculated conversion (P10s and P24s) and undersite reflection phases (p^10P, p^24P, s^10S, s^24S), respectively. The direct phase arrival times are shifted to the peak arrival rather than the onset. The multiple blue lines represent duplicates of the observed data from event S0235b. The purple lines show synthetic seismograms with a preferred source depth. RF, receiver function.
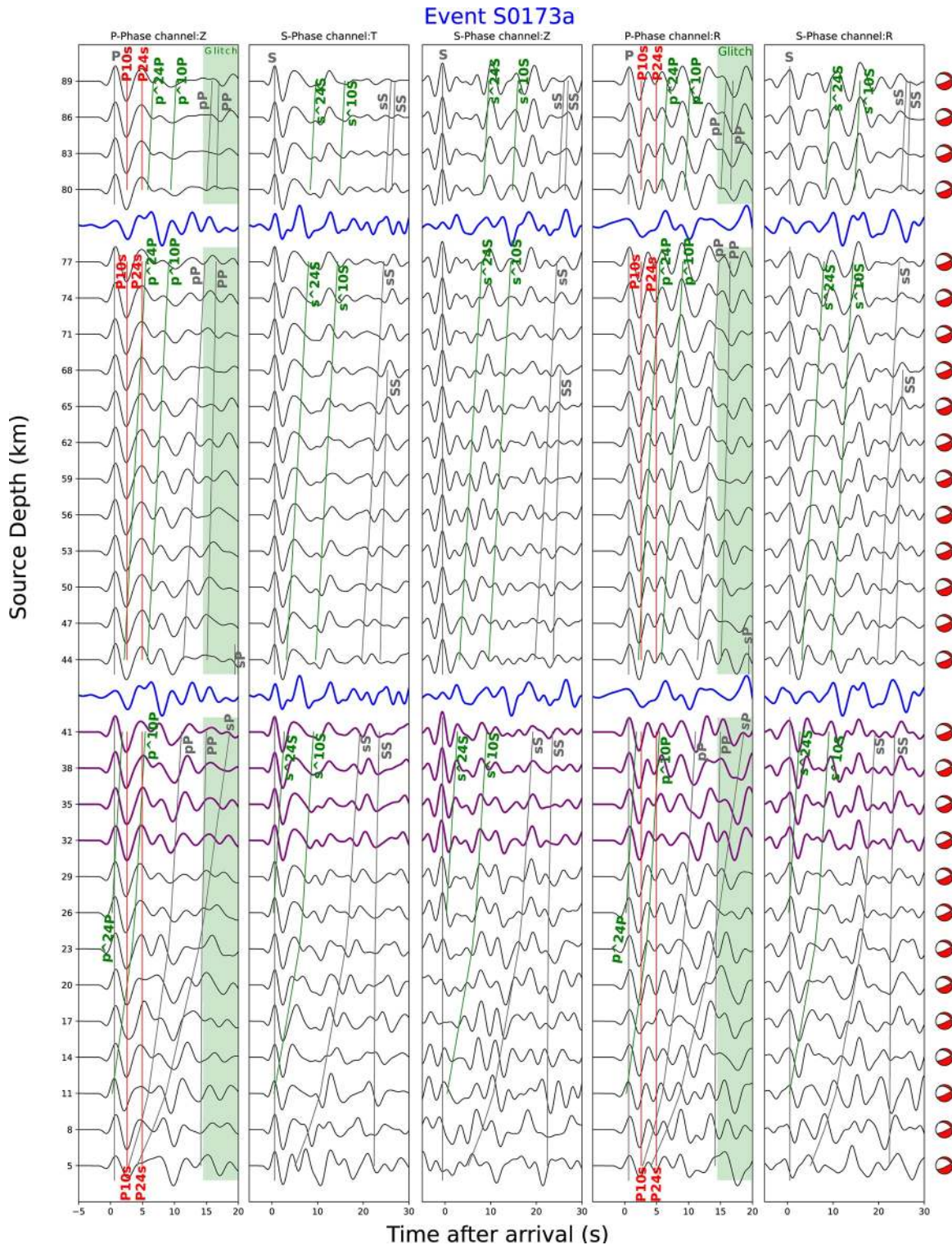
Figure D2. Synthetic seismograms (black lines) generated for the RF-constrained velocity model with the source solution shown on the right at depths ranging from 5 to 89 km in 3 km steps. From left to right the plots show the *P* wave on the vertical component (PZ), the *S* wave on the transverse component (ST), the *S* wave on the vertical component (SZ), the *P* wave on the radial component (PR), and the *S* wave on the radial component. The arrival times of the direct, depth, secondary phases (P, S, pP, sP, sS, PP, PPP, SS), based on ray theory, are shown by the gray labeled lines. The red and green labeled lines show the calculated conversion (P10s and P24s) and undersite reflection phases (p^10P, p^24P, s^10S, s^24S), respectively. The direct phase arrival times are shifted to the peak arrival rather than the onset. The multiple blue lines represent duplicates of the observed data from event S0173a. The purple lines show synthetic seismograms with a preferred source depth. The green shaded area represents the glitch recording. All seismograms are individually normalized.
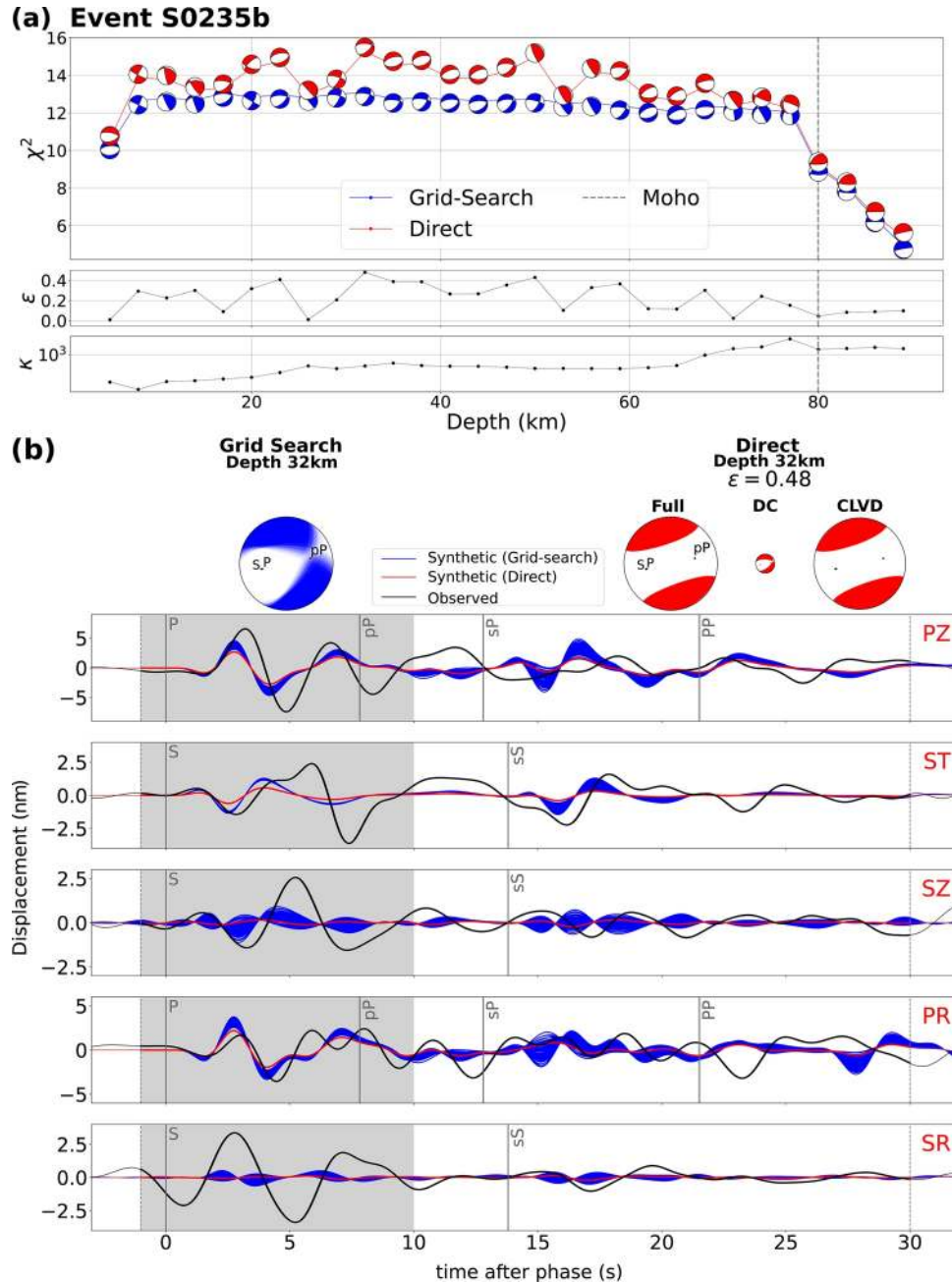
Figure E1. Inversion results for event S0235b for the TAYAK-premission model. (a) The misfit (χ^2), CLVD/DC ratio (ε) and the condition number (κ) are plotted as a function of depth. The blue and red beachballs show the source solutions for the lowest χ^2 of the GS and direct inversion, respectively. The dashed gray line denotes the depth of the Moho for the RF-constrained velocity model. (b) The solutions of the GS and direct inversion at 32 km depth shown in blue and red color, respectively. The three beachballs from the direct inversion from left to right: the full moment tensor, DC and CLVD. The DC and CLVD beachballs are scaled with respect to ε. The ray piercing-points of P, S and pP are indicated by the black dots in the beachballs. The five windows from top to bottom present the *P* wave on the vertical component (PZ), the S wave on the transverse component (ST), the *S* wave on the vertical component (SZ), the *P* wave on the radial component (PR) and the *S* wave on the radial component (SR). The gray dashed lines in the waveform plot represent the start and end of the inversion window. The light-gray area shows the higher weighted part of the waveform. The solid gray vertical lines denote the first arriving P and S phase and later arriving phases (pP, sP, PP, sS and SS) calculated using ray theory. CLVD, compensated linear vector dipole; DC, double-couple; GS, grid search.
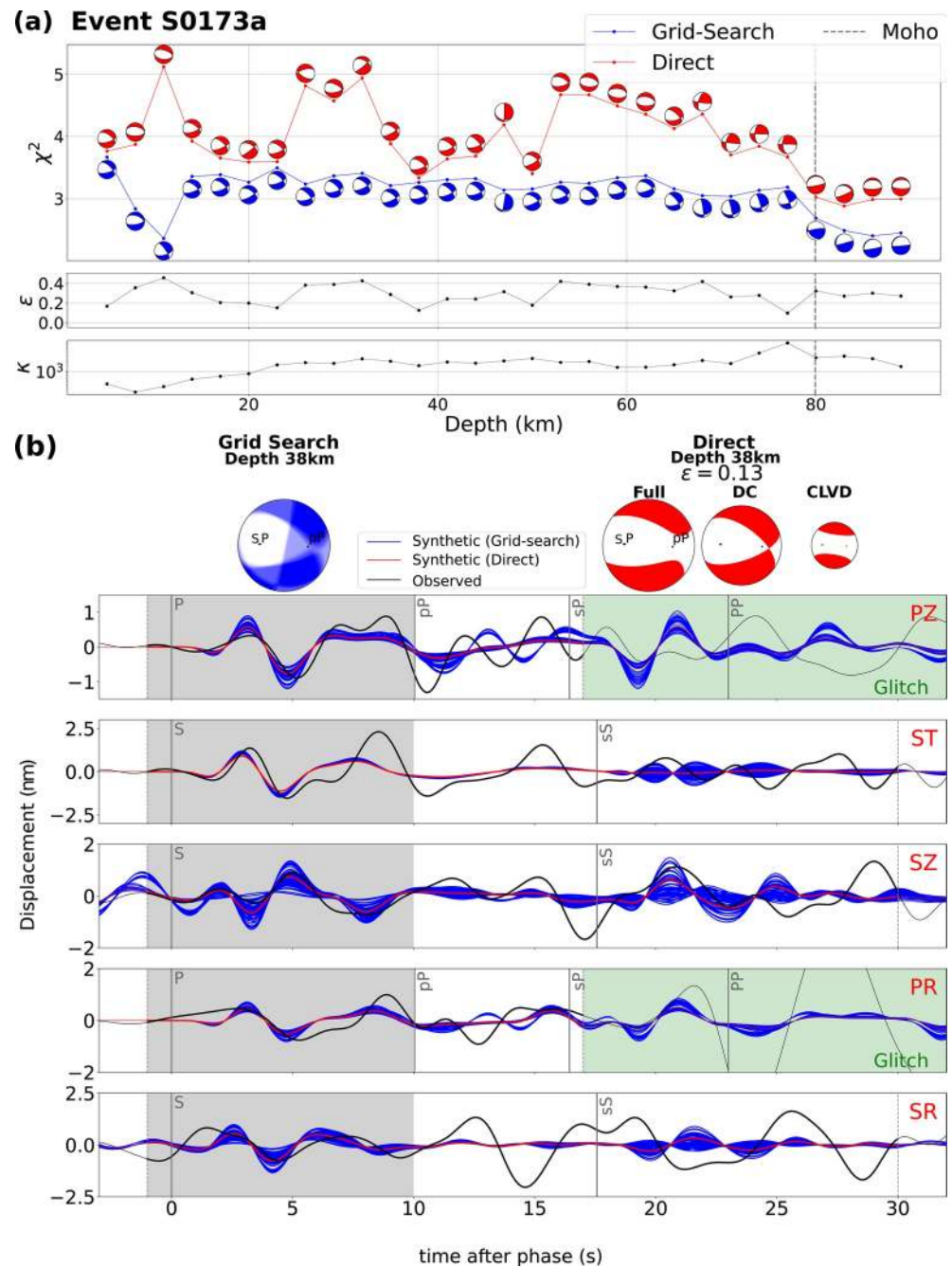
Figure E2. Inversion results for event S0173a for the TAYAK-premission model. (a) The misfit (χ^2), CLVD/DC ratio (ε) and the condition number (κ) are plotted as a function of depth. The blue and red beachballs show the source solutions for the lowest χ^2 of the GS and direct inversion, respectively. The dashed gray line denotes the depth of the Moho for the RF-constrained velocity model. (b) The solutions of the GS and direct inversion at 38 km depth shown in blue and red color, respectively. The three beachballs from the direct inversion from left to right: the full moment tensor, DC and CLVD. The DC and CLVD beachballs are scaled with respect to ε. The ray piercing-points of P, S, and pP are indicated by the black dots in the beachballs. The five windows from top to bottom present the *P* wave on the vertical component (PZ), the *S* wave on the transverse component (ST), the *S* wave on the vertical component (SZ), the *P* wave on the radial component (PR) and the *S* wave on the radial component (SR). The gray dashed lines in the waveform plot represent the start and end of the inversion window. The light-gray and green area show the higher weighted part of the waveform and the glitch, respectively. The solid gray vertical lines denote the first arriving P and S phase and later arriving phases (pP, sP, PP, sS and SS) calculated using ray theory. CLVD, compensated linear vector dipole; DC, double-couple; GS, grid search; RF, receiver function.

Data Availability Statement

Waveform data are available from the IPGP Datacenter and IRIS-DMC (InSight Mars SEIS Data Service, 2019b). Seismic waveforms are also available from NASA PDS (National Aeronautics and Space Administration Planetary Data System) (https://pds.nasa.gov/) (InSight Mars SEIS Data Service, 2019a). The terrestrial event is gfz2008ajnt in the GEOFON database (Geofon Operator, 2012), recorded at station CH.DAVOX of the Swiss Seismic Network (Swiss Seismological Service (SED) At ETH Zurich, 1983). Visualizations were created with Matplotlib (Hunter, 2007), data were processed with NumPy (Oliphant, 2007), SciPy (Virtanen et al., 2020), ObsPy (Krischer et al., 2015), and custom software developed by gempa GmbH. The source code for the moment tensor inversions and the output seismograms to produce Figures 5, 7, and 9 are made available in a public repository at https://doi.org/10.5281/zenodo.4094724

References

Aki, K., & Richards, P. G. (2002). *Quantitative seismology* (2nd ed.). University Science Books.

Banerdt, W. B., Smrekar, S. E., Banfield, D., Giardini, D., Golombek, M., & Johnson, C. L., et al. (2020). Initial results from the insight mission on mars. *Nature Geoscience*, *13*(B2), 1–7.

Böse, M., Clinton, J., Ceylan, S., Euchner, F., van Driel, M., Khan, A., et al. (2017). A probabilistic framework for single-station location of seismicity on earth and mars. *Physics of the Earth and Planetary Interiors*, *262*, 48–65.

Böse, M., Giardini, D., Stähler, S. C., Ceylan, S., Clinton, J. F., van Driel, M., et al. (2018). Magnitude scales for Marsquakes. *Bulletin of the Seismological Society of America*, *108*(5A), 2764–2777. https://doi.org/10.1785/0120180037

Buland, R., & Gilbert, F. (1976). Matched filtering for the seismic moment tensor. *Geophysical Research Letters*, *3*(3), 205–206.

Ceylan, S., Clinton, J. F., Giardini, D., Böse, M., Charalambous, C., van Driel, M., et al. (2020). Companion guide to the marsquake catalog from insight, sols 0–478: Data content and non-seismic events. *Physics of the Earth and Planetary Interiors*, *310*, 106597. https://doi.org/10.1016/j.pepi.2020.106597

Clinton, J., Ceylan, S., van Driel, M., Giardini, D., Stähler, S. C., Böse, M., et al. (2021). The marsquake catalog from insight, sols 0–478. *Physics of the Earth and Planetary Interiors*, *310*, 106595. https://doi.org/10.1016/j.pepi.2020.106595

Clinton, J., Giardini, D., Böse, M., Ceylan, S., Van Driel, M., Euchner, F., et al. (2018). The marsquake service: Securing daily analysis of seis data and building the Martian seismicity catalog for insight. *Space Science Reviews*, *214*(8), 133.

Clinton, J. F., Giardini, D., Lognonné, P., Banerdt, B., van Driel, M., Drilleau, M., et al. (2017). Preparing for insight: An invitation to participate in a blind test for martian seismicity. *Seismological Research Letters*, *88*(5), 1290–1302.

Delvaux, D., & Barth, A. (2010). African stress pattern from formal inversion of focal mechanism data. *Tectonophysics*, *482*(1–4), 105–128. http://doi.org/10.1016/j.tecto.2009.05.009

Duputel, Z., Rivera, L., Kanamori, H., & Hayes, G. (2012). W phase source inversion for moderate to large earthquakes (1990–2010). *Geophysical Journal International*, *189*(2), 1125–1147. https://doi.org/10.1111/j.1365-246X.2012.05419.x

Dziewoński, A. M., Chou, T.-A., & Woodhouse, J. H. (1981). Determination of earthquake source parameters from waveform data for studies of global and regional seismicity. *Journal of Geophysical Research*, *86*(B4), 2825–2852.

Ekström, G., Dziewonski, A. M., & Steim, J. M. (1986). Single station cmt; application to the Michoacan, Mexico, earthquake of September 19, 1985. *Geophysical Research Letters*, *13*(3), 173–176.

Ekström, G., Nettles, M., & Dziewoński, A. M. (2012). The global CMT project 2004–2010: Centroid-moment tensors for 13,017 earthquakes. *Physics of the Earth and Planetary Interiors*, *200–201*, 1–9. http://doi.org/10.1016/j.pepi.2012.04.002

Geofon, O. (2012). *Geofon event gfz2008ajnt (southern Greece; magnitude 6.5)*. Deutsches GeoForschungsZentrum GFZ. https://doi.org/10.5880/GEOFON.GFZ2008AJNT

Giardini, D., Boschi, E., & Palombo, B. (1993). Moment tensor inversion from mednet data (2) regional earthquakes of the Mediterranean. *Geophysical Research Letters*, *20*(4), 273–276.

Giardini, D., Lognonné, P., Banerdt, W. B., Pike, W. T., Christensen, U., Ceylan, S., et al. (2020). The seismicity of mars. *Nature Geoscience*, *13*(3), 205–212.

Giardini, D., Malagnini, L., Palombo, B., & Boschi, E. (1994). Broad-band moment tensor inversion from single station, regional surface waves for the 1990, NW-Iran earthquake sequence. *Annals of Geophysics*, *37*(6). https://doi.org/10.4401/ag-4157

Hardebeck, J. L., & Shearer, P. M. (2002). A new method for determining first-motion focal mechanisms. *Bulletin of the Seismological Society of America*, *92*(6), 2264–2276. https://doi.org/10.1785/0120010200

Hunter, J. D. (2007). Matplotlib: A 2d graphics environment. *Computing in Science & Engineering*, *9*(3), 90–95. https://doi.org/10.1109/MCSE.2007.55

InSight Marsquake Service. (2020). *Mars seismic catalog, insight mission; v2 2020-04-01. ETHZ, IPGP, JPL, ICL, ISAE-Supaero, MPS*. University of Bristol. https://doi.org/10.12686/a7. Retrieved from http://www.insight.ethz.ch/seismicity/catalog/v2

InSight Mars SEIS Data Service. (2019a). *InSight SEIS Data Bundle. PDS Geosciences (GEO) Node*. https://doi.org/10.17189/1517570

InSight Mars SEIS Data Service. (2019b). *SEIS raw data, Insight Mission. IPGP, JPL, CNES, ETHZ, ICL, MPS, ISAE-Supaero, LPG, MFSC*. https://doi.org/10.18715/SEIS.INSIGHT.XB\text{_}2016

Jimenez, E., Cara, M., & Rouland, D. (1989). Focal mechanisms of moderate-size earthquakes from the analysis of single-station three-component surface-wave records. *Bulletin of the Seismological Society of America*, *79*(4), 955–972.

Jost, M. U., & Herrmann, R. (1989). A student's guide to and review of moment tensors. *Seismological Research Letters*, *60*(2), 37–57.

Khan, A., & Connolly, J. (2008). Constraining the composition and thermal state of mars from inversion of geophysical data. *Journal of Geophysical Research*, *113*, E07003. https://doi.org/10.1029/2007JE002996

Khan, A., Liebske, C., Rozel, A., Rivoldini, A., Nimmo, F., Connolly, J., et al. (2018). A geophysical perspective on the bulk composition of mars. *Journal of Geophysical Research: Planets*, *123*, 575–611. https://doi.org/10.1002/2017JE005371

Khan, A., van Driel, M., Böse, M., Giardini, D., Ceylan, S., Yan, J., et al. (2016). Single-station and single-event marsquake location and inversion for structure using synthetic Martian waveforms. *Physics of the Earth and Planetary Interiors*, *258*, 28–42.

Knapmeyer, M., Oberst, J., Hauber, E., Wählisch, M., Deuchler, C., & Wagner, R. (2006). Working models for spatial distribution and level of mars' seismicity. *Journal of Geophysical Research*, *111*. E11006. https://doi.org/10.1029/2006JE002708

Krischer, L., Megies, T., Barsch, R., Beyreuther, M., Lecocq, T., Caudron, C., & Wassermann, J. (2015). Obspy: A bridge for seismology into the scientific python ecosystem. *Computational Science & Discovery*, *8*(1), 014003.

Lanczos, C. (1996). *Linear differential operators*. SIAM.

Lognonné, P., Banerdt, W. B., Giardini, D., Pike, W. T., Christensen, U., Laudet, P., et al. (2019). SEIS: Insight's seismic experiment for internal structure of mars. *Space Science Reviews*, *215*(1), 12. https://doi.org/10.1007/s11214-018-0574-6

Lognonné, P., Banerdt, W. B., Pike, W. T., Giardini, D., Christensen, U., Garcia, R. F., et al. (2020). Constraints on the shallow elastic and anelastic structure of mars from InSight seismic data. *Nature Geoscience*, *13*, 213–220. https://doi.org/10.1038/s41561-020-0536-y

Michael, A. J. (1987). Use of focal mechanisms to determine stress: A control study. *Journal of Geophysical Research*, *92*(B1), 357–368.

Minson, S. E., & Dreger, D. S. (2008). Stable inversions for complete moment tensors. *Geophysical Journal International*, *174*(2), 585–592.

Molnar, P., & Sykes, L. R. (1969). Tectonics of the Caribbean and middle America regions from focal mechanisms and seismicity. *Bulletin of the Geological Society of America*, *80*(9), 1639–1684. https://doi.org/10.1130/0016-7606(1969)80[1639:TOTCAM]2.0.CO;2

Nissen-Meyer, T., van Driel, M., Stähler, S. C., Hosseini, K., Hempel, S., Auer, L., et al. (2014). Axisem: broadband 3-d seismic wavefields in axisymmetric media. *Solid Earth*, *5*(1), 425.

Oliphant, T. E. (2007). Python for scientific computing. *Computing in Science & Engineering*, *9*(3), 10–20.

Plesa, A., Knapmeyer, M., Golombek, M. P., Breuer, D., Grott, M., Kawamura, T., et al. (2018). Present-day Mars' seismicity predicted from 3-D thermal evolution models of interior dynamics. *Geophysical Research Letters*, *45*, 2580–2589. http://doi.org/10.1002/2017GL076124

Richards, P. (1978). Basis for quantifying seismic sources from body wave data. *Transactions: American Geophysical Union*, *59*, 1139.

Rivoldini, A., Van Hoolst, T., Verhoeven, O., Mocquet, A., & Dehant, V. (2011). Geodesy constraints on the interior structure and composition of mars. *Icarus*, *213*(2), 451–472.

Roberts, G. P., Matthews, B., Bristow, C., Guerrieri, L., & Vetterlein, J. (2012). Possible evidence of paleomarsquakes from fallen boulder populations, Cerberus Fossae, Mars. *Journal of Geophysical Research*, *117*, E02009. https://doi.org/10.1029/2011JE003816

Scholz, J.-R., Widmer-Schnidrig, R., Davis, P., Lognonné, P., Pinot, B., Garcia, R. F., et al. (2020). Detection, analysis, and removal of glitches from insight's seismic data from mars. *Earth and Space Science*, *7*(11). e2020EA001317. https://doi.org/10.1029/2020EA001317

Sigloch, K., & Nolet, G. (2006). Measuring finite-frequency body-wave amplitudes and traveltimes. *Geophysical Journal International*, *167*(1), 271–287.

Smrekar, S. E., Lognonné, P., Spohn, T., Banerdt, W. B., Breuer, D., Christensen, U., et al. (2019). Pre-mission InSights on the Interior of Mars. *Space Science Reviews*, *215*(1), 3. https://doi.org/10.1007/s11214-018-0563-9

Stähler, S., & Sigloch, K. (2014). Fully probabilistic seismic source inversion-part 1: Efficient parameterization. *Solid Earth*, *5*(2), 1055–1069.

Stump, B. W., & Johnson, L. R. (1977). The determination of source properties by the linear inversion of seismograms. *Bulletin of the Seismological Society of America*, *67*(6), 1489–1502.

Swiss Seismological Service, (SED) At ETH Zürich. (1983). *National seismic networks of Switzerland*. ETH Zürich. https://doi.org/10.12686/sed/networks/ch. Retrieved from http://networks.seismo.ethz.ch/networks/ch/

Tape, W., & Tape, C. (2012). A geometric setting for moment tensors. *Geophysical Journal International*, *190*(1), 476–498.

Taylor, J., Teanby, N. A., & Wookey, J. (2013). Estimates of seismic activity in the Cerberus fossae region of Mars. *Journal of Geophysical Research: Planets*, *118*(12), 2570–2581. https://doi.org/10.1002/2013JE004469

Vallée, M., Charléty, J., Ferreira, A. M. G., Delouis, B., & Vergoz, J. (2011). SCARDEC: A new technique for the rapid determination of seismic moment magnitude, focal mechanism and source time functions for large earthquakes using body-wave deconvolution. *Geophysical Journal International*, *184*(1), 338–358. https://doi.org/10.1111/j.1365-246X.2010.04836.x

van der Kolk, D. A., Tribbett, K. L., Grosfils, E. B., Sakimoto, S. E. H., Mendelson, C. V., & Bleacher, J. E. (2001). *Orcus Patera, Mars: Impact crater or volcanic caldera?* In Lunar and planetary science conference XXXII, A-1085.

van Driel, M., Ceylan, S., Clinton, J. F., Giardini, D., Horleston, A., Margerin, L., et al. (2020). High frequency seismic events on Mars observed by InSight. *Journal of Geophysical Research: Planets*, *126*, e2020JE006670. https://doi.org/10.1029/2020JE006670

van Driel, M., Krischer, L., Stähler, S. C., Hosseini, K., & Nissen-Meyer, T. (2015). Instaseis: Instant global seismograms based on a broadband waveform database. *Solid Earth*, *6*(2), 701.

Virtanen, P., Gommers, R., Oliphant, T. E., Haberland, M., Reddy, T., & Cournapeau, D. (2020). SciPy 1.0 contributors (2020). SciPy 1.0: Fundamental algorithms for scientific computing in python. *Nature Methods*, *17*, 261–272. https://doi.org/10.1038/s41592-019-0686-2